Research Square

Preprints are preliminary reports that have not undergone peer review.
They should not be considered conclusive, used to inform clinical practice,
or referenced by the media as validated information.

Carbon-Convergent Co-utilization of Ethanol and CO2 Enables Efficient 3-Hydroxypropionic Acid Biosynthesis in Komagataella phaffii

Jianming Liu

liujianming@westlake.edu.cn

Westlake University https://orcid.org/0000-0001-6527-6049

Tong Liu

Zhejiang University

Hangbin Lei

Westlake University

Zhiqiang Chen

Westlake University

Yudian Zhu

Zhejiang University

Yongjun Mao

Westlake University

Jiacheng Feng

Westlake University

Anping Zeng

Westlake University

Article

Keywords:

Posted Date: October 27th, 2026

DOI: https://doi.org/10.21203/rs.3.rs-11458557/v1

License: This work is licensed under a Creative Commons Attribution 4.0 International License.
Read Full License

Additional Declarations: There is **NO** Competing Interest.

Carbon-Convergent Co-utilization of Ethanol and CO_2 Enables Efficient 3-Hydroxypropionic Acid Biosynthesis in *Komagataella phaffii*

Tong Liu[1,2,3], Hangbin Lei[2,4], Zhiqiang Chen[2], Yudian Zhu[1,2,3], Yongjun Mao[2,3], Jiacheng Feng[2,3], Jianming Liu[*2,5,6] and An-Ping Zeng[*2,3,4,5,6]

1. Zhejiang University, Hangzhou, Zhejiang, China
2. Center of Synthetic Biology and Integrated Bioengineering, Westlake University, Hangzhou, Zhejiang, China
3. School of Engineering, Westlake University, Hangzhou, Zhejiang, China
4. School of Life Sciences, Westlake University, Hangzhou, Zhejiang, China
5. Research Center for Industries of the Future, Westlake University, Hangzhou, Zhejiang, China
6. Key Laboratory of Intelligent Low-Carbon Biosynthesis of Zhejiang Province , Westlake University, Hangzhou, Zhejiang, China

* Correspondence: Dr. Jianming Liu, liujianming@westlake.edu.cn

Dr. An-Ping Zeng, zenganping@westlake.edu.cn

Abstract

CO_2 is an abundant feedstock for biomanufacturing, but its high oxidation state demands substantial reducing power for multicarbon biosynthesis. Here, we establish a carbon-convergent strategy for producing 3-hydroxypropionic acid (3-HP) through the co-utilization of ethanol and inorganic carbon in engineered *Komagataella phaffii*. Ethanol serves as a nexus molecule that supplies a conserved C2 backbone together with reducing equivalents, enabling a "2+1=3" route to 3-HP through inorganic C1 incorporation. Coordinated engineering of ethanol assimilation, acetate activation, carboxylation, cofactor supply, and energy metabolism generated strain LT-28, which produced 127.04 g/L 3-HP, the highest titer reported so far for CO_2-based biosynthesis. ^{13}C tracing verified the joint contribution of ethanol-derived C2 carbon and inorganic C1 carbon to the product skeleton. LT-28 also converted an unpurified ethanol-rich stream from thermocatalytic CO_2 reduction into 3-HP. These findings demonstrate the feasibility of coupling chemical CO_2 reduction with microbial 3-HP biosynthesis through ethanol-mediated carbon convergence.

Introduction

Carbon dioxide (CO_2) is an abundant C1 feedstock for sustainable synthesis of chemicals, but its conversion into reduced multicarbon products requires substantial energy and reducing equivalents[1-5]. Powered by renewable energy, chemical and electrochemical catalysis can reduce CO_2 into energy-rich intermediates, while biological systems offer high selectivity and access to complex multistep transformations[4,6-8]. Hybrid chemical–biological platforms therefore provide an attractive route for combining the strengths of both catalytic regimes[4,7,8]. However, chemically generated intermediates are primarily considered as carbon carriers, although their redox state, carbon atom economy and metabolic compatibility can be equally important determinants of overall process performance[9,10]. An effective nexus molecule should therefore not only connect chemical CO_2 conversion with microbial metabolism, but also supply carbon and reducing power in a form aligned with the energetic and biosynthetic demands of the target product.

This consideration is particularly relevant for the synthesis of 3-hydroxypropionic acid (3-HP), a versatile C3 platform chemical identified by the U.S. Department of Energy as one of the most promising value-added building blocks. Owing to its two functional groups, 3-HP can serve as a precursor for acrylic acid, acrylamide, 1,3-propanediol, biodegradable polymers and other commodity and specialty chemicals. Its sustainable production is therefore of considerable industrial interest. Among the available biosynthetic routes, the malonyl-CoA pathway is especially attractive because it combines an acetyl-CoA-derived C2 unit with an inorganic C1 unit. However, this pathway also requires substantial reducing power, as the conversion of malonyl-CoA to 3-HP consumes approximately two NAD(P)H equivalents[11,12]. Previous 3-HP production strategies have mainly relied on reduced organic substrates such as glucose or glycerol[13-18], and extensive metabolic engineering has improved titer by strengthening acetyl-CoA and malonyl-CoA supply, balancing pathway expression and reducing competing fluxes[19]. Nevertheless, these approaches remain largely rooted in conventional sugar-based metabolism and do not explicitly exploit the potential complementarity between a reduced C2 substrate and an inorganic C1 unit[19,20]. We therefore propose that a more carbon-efficient route could be established by combining a highly reduced C2 intermediate with biological carboxylation, allowing two carbon atoms to be supplied through the reduced substrate and a third carbon to be incorporated. In this approach, the optimal precursor is not simply the substrate that reaches acetyl-CoA most readily, but the one whose carbon content and reducing equivalents are collectively matched to the requirements of 3-HP biosynthesis. Ethanol satisfies these requirements particularly well. It is a reduced C2 molecule that can be generated from CO_2 through chemical routes[21-23], while its oxidation to acetyl-CoA conserves both carbon atoms and generates NADH, thereby coupling carbon assimilation to reducing-power and respiratory-energy generation[24]. This metabolic architecture creates a "2+1=3" carbon-convergent pathway: ethanol supplies the C2 backbone of acetyl-CoA, acetyl-CoA carboxylase 1 (ACC1) incorporates an additional inorganic carbon to form malonyl-CoA, and malonyl-CoA reductase converts this C3 intermediate into 3-HP[11]. This pathway illustrates how reduced

intermediates supplying both carbon and metabolic energy can facilitate inorganic-carbon assimilation in hybrid CO_2 conversion.

Here, we establish a carbon-convergent CO_2-to-3-HP platform by coupling thermocatalytic CO_2-to-ethanol conversion with engineered *Komagataella phaffii* (formerly *Pichia pastoris*). Guided by a multidimensional evaluation of CO_2-derived intermediates, we identified ethanol as a redox- and carbon-compatible nexus molecule and engineered *K. phaffii* for efficient ethanol assimilation, carboxylation and 3-HP synthesis. The resulting strain produced 127.04 g/L 3-HP, representing, to our knowledge, the highest titer reported so far for de novo microbial 3-HP production, while ^{13}C tracing demonstrated that the C3 product skeleton arises from an ethanol-derived C2 unit and an ACC1-fixed inorganic C1 unit. Together, these results establish a carbon-convergent co-utilization strategy in which reduced C2 intermediates and inorganic carbon are jointly exploited for multicarbon biosynthesis.

Results

Multidimensional evaluation identifies ethanol as a balanced nexus molecule for CO_2 co-utilization

We selected 3-HP as the target product for evaluating which CO_2-derived nexus molecule could effectively support the simultaneous carbon incorporation and reductive biosynthesis. To establish a rational basis for nexus-molecule selection in a hybrid CO_2 valorization system, we constructed a multidimensional approach comparing representative C1 and C2 intermediates according to their assimilation pathways, carbon atom economy, cofactor balance for 3-HP synthesis and microbial biocompatibility (**Fig. 1a**). This approach connects the catalytic accessibility of each intermediate with its downstream metabolic performance, thereby evaluating its suitability for integrating chemical CO_2 conversion with microbial biosynthesis.

Representative assimilation routes for formate, methanol and methane involve approximately 8–11 steps to acetyl-CoA, compared with one step for acetate and three for ethanol (**Fig. 1a**)[10]. Formate and methane provide insufficient reducing equivalents for subsequent 3-HP synthesis, whereas methanol shows a predicted surplus but requires a longer assimilation route. Acetate offers high carbon retention and direct access to acetyl-CoA but generates no net reducing equivalents, while ethylene lacks a well-established microbial route to acetyl-CoA. In contrast, ethanol combines high carbon retention with a short assimilation route and generates approximately two reduced nicotinamide cofactors during its conversion to acetyl-CoA, potentially contributing to the two NADPH molecules required for 3-HP biosynthesis[24,25]. Furthermore, ethanol can be produced from CO_2 through thermocatalytic or electrochemical reduction using renewable hydrogen or electricity[23]. These properties motivate a hybrid "2+1=3" approach in which CO_2-derived ethanol supplies the C2 backbone, while direct inorganic-carbon incorporation contributes the third carbon of

3-HP (**Fig. 1b**).

Comparative screening identifies, *K. phaffii* GS115 as a balanced ethanol-assimilating chassis

Having identified ethanol as a potentially balanced nexus molecule for the carbon-convergent synthesis of 3-HP, we next sought to identify a microbial chassis capable of efficiently converting ethanol into acetyl-CoA (**Fig. 2a**)[26,27]. We evaluated six representative yeast strains (*K. phaffii* GS115, *Yarrowia lipolytica* PO1f, *Rhodotorula toruloides* NP11, *Saccharomyces cerevisiae* BY4741, *Ogataea polymorpha* NCYC495, and *S. cerevisiae* CEN.PK2-1C) for their ability to utilize ethanol as a sole carbon source. In shake-flask cultivation with 10 g/L ethanol, *K. phaffii* GS115 displayed rapid growth, reaching an OD_{600} of about 2.5 at 12 h and maintaining robust growth through 48 h (**Fig. 2b**). This rapid proliferation was coupled with superior substrate consumption, as *K. phaffii* GS115 depleted ethanol faster than the most strains tested, reducing ethanol levels to near 1 g/L within 48 h (**Fig. 2c**). Detailed fermentation kinetic profiles over 120 h further corroborated these observations (**Extended Data Fig. 1a-f**). Notably, *K. phaffii* GS115 achieved a high biomass yield (approaching 0.9 g cell/g ethanol) while producing negligible maximum acetate accumulation (0.1 g/L), in strong contrast to strains like *O. polymorpha* NCYC495 and *S. cerevisiae* CEN.PK2-1C which accumulated over 0.8 g/L acetate (**Fig. 2d**)[28]. *S. cerevisiae* BY4741 also exhibited rapid initial ethanol uptake and a high biomass yield (**Fig. 2b, d and Extended Data Fig. 1a-f**). However, when evaluated on 3 g/L acetate medium, BY4741 showed strongly impaired growth and slow acetate clearance (**Fig. 2e**). In contrast, GS115 exhibited the highest cell density and rapid acetate clearance, confirming its superior metabolic capacity for C2 intermediate assimilation (**Fig. 2e**).

To investigate the transcriptional basis associated with these phenotypic differences, we performed principal component analysis (PCA) of global transcriptomic profiles obtained under ethanol cultivation. PCA revealed distinct transcriptomic profiles among the six strains, with GS115 occupying a separate position in the PC1–PC2 space (PC1, 36.08%; PC2, 23.24%) (**Fig. 2f**). Comparison of selected metabolism-related genes further revealed differences between rapid upstream ethanol oxidation and balanced downstream carbon assimilation. BY4741 showed relatively higher expression of *ADH*, *ALD* and *ACS* but lower expression of *PCK1* and *PGI1* in the row-scaled heatmap (**Fig. 2g**). This transcriptional pattern is consistent with its rapid ethanol consumption but limited growth on acetate. By contrast, GS115 combined moderate expression of upstream ethanol-oxidation genes with higher expression of genes involved in acetyl-CoA assimilation, the glyoxylate cycle, the tricarboxylic acid cycle and gluconeogenesis, including *PGI1*, *PCK1*, *MLS1*, *ACO1* and *KGD1* (**Fig. 2g**). When GS115 was shifted to acetate medium, the expression of acetyl-CoA synthetase and the glyoxylate-cycle-associated genes *MLS1* and *PCK1* increased further, consistent with its efficient acetate metabolism. GS115 also showed comparatively high expression of genes associated with membrane integrity and lipid metabolism, including *OLE1*, *OLE2*, *FAS1* and *FAS2*, which may contribute to its ability to withstand multiple stress (**Fig. 2g**)[29,30]. Collectively, the growth and substrate-utilization results support GS115 as a suitable host for ethanol-based biosynthesis. We therefore selected GS115 for construction of the ethanol-driven 3-HP

pathway.

Substrate-dependent flux imbalance identifies acetate activation as a constraint on C2 assimilation

Having selected GS115 as the ethanol-assimilating chassis, we next constructed the "2+1=3" route by coupling its native ethanol-assimilation pathway with heterologous 3-HP biosynthesis pathway. In this architecture, ethanol is sequentially oxidized to acetaldehyde and acetate before conversion to acetyl-CoA. ACC1-dependent carboxylation then incorporates an additional inorganic carbon into acetyl-CoA to generate malonyl-CoA, which is reduced by malonyl-CoA reductase (MCR) to form 3-HP (**Fig. 3a**). To identify the endogenous gene-determinants governing ethanol-derived carbon assimilation in GS115, we systematically disrupted seven candidate genes involved in ethanol oxidation, acetaldehyde conversion and acetate activation (**Fig. 3b**). They include alcohol dehydrogenases (*ADH2*, *ADH6*, *ADH7* and *ADH900*)[31,32], aldehyde dehydrogenase (*ALD1*)[25], and acetyl-CoA synthetases (*ACS1* and *ACS2*)[24,25]. Under an initial ethanol concentration of 20 g/L, the parental GS115 strain consumed approximately 98% of the ethanol within 72 h, whereas deletion of *ADH2*, *ALD1* or *ACS1* reduced ethanol consumption to 22%, 23% and 16%, respectively (**Fig. 3b**). In contrast, deletion of *ADH6*, *ADH7*, *ADH900* or *ACS2* showed substantially weaker effects, indicating functional redundancy or minor contributions under ethanol cultivation conditions. This systematic comparison revealed the *ADH2–ALD1–ACS1* axis as the dominant route directing ethanol-derived carbon into the acetyl-CoA pool.

We next optimized the heterologous 3-HP module by tuning transcriptional balance between pathway enzymes. A GFP-based promoter characterization under ethanol cultivation conditions revealed distinct expression strengths among native promoters (**Supplementary Fig. 1**). We evaluated six promoter combinations to independently regulate the expression between the C-terminal and N-terminal catalytic domains of malonyl-CoA reductase (*MCR-C* and *MCR-N*, respectively)[11,33,34] , across 5, 10 and 20 g/L ethanol (**Fig. 3c**). Here, *MCR-C* represents an engineered *MCR-C* variant (N940V/K1106W/S1114R) previously reported to improve 3-HP biosynthesis[11,33]. Among the tested combinations, strain LT-13 in which *MCR-N* was controlled by GAPp and *MCR-C* by ADH2p, yielded the maximum 3-HP titer at all tested ethanol concentrations, with approximately 1.4 g/L 3-HP at 20 g/L ethanol (**Fig. 3c**). We therefore selected strain LT-13 as the optimized ethanol-driven chassis for further engineering.

To further evaluate whether increasing ethanol assimilation capacity could improve carbon conversion, we overexpressed ADH2, ALD1 and ACS1 in strain LT-13, generating strains LT-14 to LT-18 with different ACS1 promoter strengths (**Fig. 3d**). Under high ethanol loading (20 g/L), these modifications produced only modest differences in residual ethanol and 3-HP formation after 72 h cultivation, although acetate had already begun to accumulate in several strains. More pronounced differences emerged after 120 h. Strains LT-16, LT-17 and LT-18 showed greater ethanol depletion, while LT-16, LT-17

reached approximately 0.9-1.0 g/L 3-HP, compared with approximately 0.7-0.8 g/L in LT-13 and LT-14 (**Fig. 3d**). Interestingly, increasing ACS1 expression (strain LT-18) did not proportionally improve 3-HP formation. Instead, excessive enhancement of the upstream ethanol-to-acetate flux resulted in increased acetate accumulation, indicating that carbon delivery into the acetate pool exceeded the capacity for subsequent acetyl-CoA generation (**Fig. 3d**). By contrast, at lower ethanol concentrations (1–10 g/L), overexpression of *ADH2*, *ALD1* and *ACS1* produced only limited improvements in ethanol consumption and 3-HP production (**Extended Data Fig. 2**), indicating that the benefit of enhanced ethanol assimilation became more evident under high substrate loading. Among the engineered strains, strain LT-16 achieved the highest 3-HP titer with the lowest acetate accumulation (**Fig. 3d**), suggesting that optimal carbon conversion required a balance between ethanol assimilation and acetate activation rather than simply maximizing upstream flux.

ACS1 enzyme engineering

Given the critical role of acetate activation in the ethanol-to-3-HP conversion, we sought to improve this step by engineering the endogenous acetyl-CoA synthetase ACS1. We combined Saprot-based protein language model prediction with MD- and literature-guided semi-rational design to generate ACS1 variants[35-37], and evaluated their activities. Among the tested variants, I658P showed the largest improvement, increasing relative ACS1 activity to approximately 150% of ACS1wt (**Fig. 4a**), whereas most variants showed limited or no enhancement (**Extended Data Fig. 3a, b**). We next combined I658P with several beneficial substitutions, but none of these combinations outperformed I658P alone (**Fig. 4b**). These results identified ACS1-I658P as the optimal variant for further characterization.

Purified ACS1-I658P exhibited higher acetyl-CoA formation rates than ACS1wt across the tested acetate concentrations (**Fig. 4c**). Kinetic analysis showed that I658P increased V_{max} from 38.40 ± 0.86 to 45.74 ± 0.99 μmol $min^{-1}mg^{-1}$ and K_{cat} from 47.29 ± 1.06 to 56.34 ± 1.21 s^{-1}, while the apparent K_m for acetate remained nearly unchanged (**Supplementary Table 8**). Consequently, catalytic efficiency increased from 426.1 ± 39.6 to 526.5 ± 45.7 $mM^{-1}s^{-1}$, indicating that I658P primarily improves catalytic turnover rather than acetate affinity. Consistent with this enhanced catalytic performance, ACS1-I658P also supported higher 3-HP production than the reported *Salmonella enterica* ACS-L641P variant when evaluated in our ethanol-to-3-HP system[38,39] (**Fig. 4d**).

Structural studies have shown that ACS catalysis involves substantial reorganization of the C-terminal domain and that a conserved lysine is essential for the adenylation reaction and can be inactivated by acetylation[35]. In *S. enterica*, mutation of the nearby L641 residue prevents Pat-dependent acetylation of K609 and maintains ACS in an active state[36]. Sequence alignment placed K626 and I658 of *K. phaffii* GS115 ACS1 in the corresponding region, suggesting that I658P might alter the accessibility of K626 to acetylation. To examine this hypothesis, we performed molecular dynamics simulations

of ACS1 in complex with a GNAT acetyltransferase domain and acetyl-CoA. Across eight independent 500-ns simulations, the mean distance between the K626 side-chain amine and the acetyl carbonyl carbon increased from 6.60 ± 1.41 Å in ACS1wt to 8.99 ± 1.53 Å in ACS1-I658P (**Fig. 4e**). Moreover, acetylation-compatible near-attack geometries were detected in ACS1wt, whereas no productive frames were observed across the eight ACS1-I658P trajectories (**Fig. 4f, g**), whereas the fraction of frames in which K626 was oriented towards acetyl-CoA showed a modest decrease in I658P (**Extended Data Fig. 3c**). Representative snapshots further illustrated this orientational difference, with K626 adopting a toward-ACO orientation in ACS1wt (CE–NZ–C=128°) but an away-from-ACO orientation in ACS1-I658P (25°) (**Extended Data Fig. 3d**).

Coordinated metabolic engineering enables ethanol-CO_2 co-utilization for 3-HP synthesis

We next systematically engineered *K. phaffii* to improve ethanol utilization and 3-HP synthesis. Rather than eliminating the native acetyl-CoA- and malonyl-CoA-consuming pathways, we retained the original glyoxylate cycle, TCA cycle and fatty-acid synthesis to support biomass formation, energy generation and membrane integrity, while selectively reinforcing ethanol oxidation, acetate activation, CO_2 fixation, NADPH supply and 3-HP synthesis (**Fig. 5a**). In this design, the two carbon atoms of ethanol are retained in acetyl-CoA, whereas ACC1-dependent carboxylation incorporates an additional inorganic carbon to generate the C3 precursor malonyl-CoA, thereby coupling C2 assimilation with C1 incorporation for 3-HP synthesis[11]. To implement this design, we constructed eight progressively engineered strains and evaluated them during 160 h ethanol fed-batch shake-flask cultivation. Although initial reinforcement of ethanol oxidation in strain LT-14 to LT-16 reduced biomass formation and 3-HP production, subsequent pathway balancing progressively restored productive flux (**Fig. 5b and Extended Data Fig. 4**). Replacing chromosomally integrated ACS1wt in strain LT-16 with ACS1-I658P increased the final 3-HP titer from 0.79 to 1.09 g/L, corresponding to a 38.5% improvement and confirming its beneficial effect. Introduction of ACC1 produced the largest subsequent gain, increasing 3-HP production to 2.05 g/L and identifying acetyl-CoA carboxylation as another major control point connecting ethanol-derived C2 metabolism with inorganic-carbon incorporation[40]. Further pathway reinforcement increased the final 3-HP titer to 2.79 g/L in strain LT-28, approximately 50% higher than 1.86 g/L obtained with strain LT-13. Time-course profiles further showed greater 3-HP accumulation in strain LT-28 than in LT-13 (**Fig. 5c and Extended Data Fig. 4**). Strain LT-28 was therefore selected for physiological characterization and bioreactor cultivation.

We next examined how progressive engineering affected the distribution of ethanol-derived carbon. Acetate accumulated strongly in several intermediate strains but was markedly reduced in the later engineered strains and was nearly depleted in strain LT-28 at 160 h (**Fig. 5d**), indicating increasingly efficient capture of ethanol-derived carbon downstream of acetate. Intracellular acetyl-CoA increased substantially following reinforcement of acetate activation and remained elevated in the later strains (**Fig. 5f**).

This pattern suggests that productive pathway engineering requires efficient acetyl-CoA turnover rather than simply maximizing its intracellular accumulation[41,42]. The intracellular glutathione profile was also substantially remodelled across the strain series (**Fig. 5e**), consistent with altered redox demand during intensified ethanol assimilation and 3-HP biosynthesis[27,43]. Adenylate profiling revealed a concomitant redistribution of ATP, ADP and AMP pools during pathway engineering (**Extended Data Fig. 5a–c**). Accordingly, the adenylate energy charge increased markedly after reinforcement of ethanol assimilation and remained significantly higher in strain LT-28 than in the early-stage strain LT-13 despite the increased energetic demands of 3-HP production (**Fig. 5g**). Because small-molecular organic alcohols and organic acids can perturb the organization and permeability of microbial plasma membranes[27,30,44-46], we further examined cell integrity during fed-batch cultivation. At 48 h, Propidium Iodide (PI) staining revealed substantially lower membrane damage in several of the progressively engineered strains, including LT-28, than in the early production strains (**Fig. 5h, i and Extended Data Fig. 5d**). However, by 144 h, the proportion of PI-positive cells approached saturation across the strain series, indicating severe late-stage loss of membrane integrity under prolonged ethanol feeding without pH control. This deterioration coincided with the pronounced slowing of 3-HP accumulation after approximately 96 h, indicating that cellular stress might become a major constraint during late-stage shake-flask cultivation.

Process optimization enables high-titer 3-HP production from ethanol and CO_2

The late-stage loss of membrane integrity observed during shake-flask cultivation suggested that the production capacity of LT-28 was constrained by the cultivation environment. We therefore evaluated LT-28 under controlled fed-batch conditions. An initial fermentation produced approximately 120 g/L 3-HP, but required nearly 280 h (**Extended Data Fig. 6a**). We therefore optimized continuous aeration, pH control at 5.6 and DO-responsive ethanol feeding. Under the optimized process, strain LT-28 accumulated 127.04 g/L 3-HP within 157 h (**Fig. 6a**). Compared with representative microbial 3-HP production systems using methanol[47,48], glucose[13-15], glycerol[16,17], lignocellulosic substrates[49,50] and other carbon sources[18,51] (**Fig. 6b and Supplementary Table 10**), to our knowledge, this represents the highest titer for de novo microbial 3-HP production (**Fig. 6b**). LT-28 simultaneously reached a maximum dry cell weight (DCW) of 125.82 g/L at 109 h and retained 102.22 g/L at 157 h, demonstrating high-cell-density growth on ethanol throughout the production phase (**Extended Data Fig. 6b**).

We next examined whether controlled fermentation mitigated the loss of cellular integrity observed in shake flasks. PI-positive cells accounted for approximately 32% of the population at 85 h and remained below approximately 40% at 157 h, rather than approaching population-wide staining as observed during prolonged shake-flask cultivation without pH control (**Fig. 6c and Extended Data Fig. 6f**). Thus, maintenance of pH 5.6 substantially prolonged population viability during high-titer production. SEM imaging nevertheless revealed progressive morphological damage, with a subset of cells developing surface depressions and collapsed structures at 85 and 157 h, while a considerable fraction retained an intact morphology (**Fig. 6d**). These observations

indicate that ethanol-associated cellular stress persisted during the optimized fermentation but did not cause population-wide structural failure.

To trace the carbon origin of 3-HP produced from ethanol, we performed ^{13}C-labelling experiments with [U-$^{13}C_2$] ethanol and $NaH^{13}CO_3$ (**Supplementary Table 9**). After 6 h, [U-$^{13}C_2$] ethanol predominantly enriched the M+2 isotopologue of 3-HP, $NaH^{13}CO_3$ predominantly enriched M+1, and combined labelling produced a pronounced M+3 signal (**Fig. 6e**). Notably, in the absence of exogenous $NaHCO_3$, [U-$^{13}C_2$] ethanol also gave rise to a substantial M+3 fraction, consistent with rapid incorporation of CO_2 generated during the oxidative metabolism of ethanol into 3-HP.

To further assess whether exogenous inorganic carbon could enhance ethanol-based 3-HP production, we compared fed-batch fermentations of LT-28 with or without $NaHCO_3$ supplementation (**Extended Data Fig. 7a, b**). At 111 h, $NaHCO_3$ supplementation increased the 3-HP titer from 78.87 to 95.26 g/L, representing a 20.8% increase. Cumulative ethanol feeding was comparable between the control and $NaHCO_3$-supplemented cultures (160.8 g and 167.4 g, respectively), with residual ethanol concentrations below 1 g/L in both cultures at the final sampling point. These results suggest that supplementation with inorganic carbon can further enhance ethanol-based 3-HP production.

To characterize the physiological state associated with high-titer production, we compared LT-28 with LT-13 by quantitative proteomics. A total of 349 proteins were upregulated and 603 were downregulated in LT-28 (**Fig. 6f**). The abundance of ADH2, ALD1 and ACS1 increased substantially, consistent with reinforcement of the ethanol-to-acetyl-CoA pathway. AOX1 and AOX2 were also strongly upregulated, indicating broader remodelling of peroxisome-associated metabolism[30,52]. The putative GPI-anchored protein (PAS_chr3_0516) was strongly increased, consistent with activation of cell-surface remodelling processes under prolonged ethanol stress[53]. In contrast, FAS1 and FAS2 were downregulated, whereas intracellular glycerol-3-phosphate increased strongly, suggesting altered lipid metabolism rather than a simple increase in fatty-acid synthesis (**Fig. 6f, h**). Consistent with this interpretation, LT-28 exhibited extensive redistribution of individual lipid species across multiple lipid classes despite largely unchanged global membrane-lipid indices (**Extended Data Fig. 8a-c**). This compositional redistribution may reflect lipid adaptation to prolonged ethanol exposure. KEGG enrichment further highlighted oxidative phosphorylation, glycerolipid metabolism, glutathione metabolism, the TCA cycle, glyoxylate and dicarboxylate metabolism, glycolysis/gluconeogenesis and the pentose phosphate pathway (**Fig. 6g**). Extracellular carbohydrate concentrations, which gradually rose throughout fermentation to approximately 2.5 g/L at 157 h (**Extended Data Fig. 6c**), were dominated by a low-molecular-weight fraction accounting for 96.66% (**Extended Data Fig. 6d, e**), consistent with the broad carbon redistribution toward gluconeogenic and carbohydrate metabolism observed in LT-28. Metabolite profiling further revealed coordinated enhancement of central carbon, redox and energy metabolism in LT-28. Acetyl-CoA, citrate, fumarate and glucose-6-phosphate were all

elevated, while glycerate and glycerol-3-phosphate also increased markedly, consistent with redistribution of ethanol-derived carbon through central and gluconeogenic metabolism (**Fig. 6g, h and Extended Data Fig. 6h**). Intracellular NADH and NADPH increased substantially despite expression of the NADH-consuming POS5 module, indicating that reducing-equivalent generation remained high in LT-28. Because ethanol oxidation through ADH2 and ALD1 generates NADH, the elevated NADH pool is consistent with strong upstream ethanol-oxidation capacity, while POS5 provides an ATP-dependent route for converting NADH-derived reducing power into NADPH[54]. ATP and ADP increased whereas AMP decreased, while the total adenylate pool remained nearly unchanged, causing the adenylate energy charge to rise from approximately 0.22 in LT-13 to 0.37 in LT-28 (**Fig. 6h and Extended Data Fig. 6h, i**). The simultaneous enrichment of oxidative phosphorylation and redistribution of adenylates towards ATP therefore indicate a more highly phosphorylated cellular energy state in LT-28. Conversely, metabolites decreased in LT-28 were enriched in nucleotide, purine and pyrimidine metabolism (**Extended Data Fig. 6g**). AMP, guanosine, cAMP, cGMP and uracil were among the representative depleted metabolites (**Extended Data Fig. 6i**), indicating selective redistribution of nucleotide pools rather than generalized metabolite accumulation. Together, these results establish LT-28 as a high-cell-density, high-flux ethanol-utilizing chassis in which enhanced carbon assimilation, reducing-power generation and cellular energy metabolism support record de novo 3-HP production.

Biosynthesis of 3-HP from CO_2

To further establish a CO_2-to-3-HP production route, we coupled thermocatalytic CO_2 conversion with biosynthesis with the best-performing engineered strain LT-28 (**Extended Data Fig. 9a**). The upper- and lower-layer catalysts were characterized by high-resolution transmission electron microscopy and elemental mapping, confirming the corresponding crystalline phases and elemental distributions in both catalyst layers (**Extended Data Fig. 9b, c**). The dual-bed thermocatalytic system converted CO_2-containing gas mixtures into a liquid product stream dominated by ethanol, with ethanol accounting for up to 81.2% of the liquid products under gas mixture 1 (**Fig. 7a**).

The collected thermocatalytic liquid was subsequently supplied directly to the LT-28 bioreactor without intermediate purification or separation. During the 4 h coupled conversion, the thermocatalytic liquid containing 69.94 g/L ethanol yielded 3-HP at 0.476 g/g ethanol consumed, with an average productivity of 0.21 g/L/h and negligible residual ethanol (**Extended Data Fig. 9d**). Comparison with previously reported electrochemical–biological or chemical–biological CO_2 conversion systems showed that this productivity exceeded those reported for the production of lipids[55], glucose and fatty acids[56], biomass[57], PHA[58], tyrosine[59], PHB[60,61] and ectoine[62] (**Fig. 7b and Supplementary Table 11**). Together, these results establish a previously unreported end-to-end thermochemical–biological route from CO_2 to 3-HP, while maintaining a comparatively high overall productivity.

To evaluate the economic feasibility and environmental performance of the integrated

CO_2-to-3-HP process, we performed a techno-economic analysis (TEA) and life-cycle assessment (LCA) based on an Aspen Plus process model[63-65] (**Fig. 7c and Supplementary Fig. 2**). The process was designed for an annual production capacity of 5,000 t 3-HP, with an overall downstream recovery of 78.1% and a final product specification of 30% (w/v) aqueous 3-HP solution [66](**Supplementary Table 12**).

The annual operating expenditure (OPEX) was US$3.23 million/year after accounting for co-product credits (**Fig. 7d and Supplementary Table 15**). Raw materials and utilities contributed US$8.75 million/year, of which captured CO_2, solar power and H_2 accounted for 52.57%, 24.57% and 18.51%, respectively. Credits from single-cell protein (SCP) and carbon taxation reduced the annual cost by US$8.43 million/year. The minimum selling price (MSP) of 3-HP was US$1.07/kg under the base-case conditions. Single-point sensitivity analysis was performed by varying the prices of major raw materials, utilities and the SCP co-product by ±20% relative to their base-case values (**Fig. 7e**). The MSP was most sensitive to the SCP and CO_2 prices, with corresponding variations of −5.6% to +8.4% and −3.7% to +6.5%, respectively. H_2 and solar-power prices produced smaller but appreciable changes, whereas variation in 3-HP titer had a comparatively limited effect on the MSP.

For the LCA, environmental impacts were normalized to 1 kg pure 3-HP equivalent. The global warming potential (GWP) of the integrated process was 1.39 kg CO_2-eq/kg 3-HP after accounting for the SCP co-product credit (**Fig. 7f and Supplementary Table 16**). H_2 supply and direct CO_2 emissions contributed 7.08 and 5.76 kg CO_2-eq, respectively, whereas CO_2 inflow contributed −9.99 kg CO_2-eq and the SCP co-product contributed −2.10 kg CO_2-eq. Solar electricity and water contributed 0.62 and 0.02 kg CO_2-eq, respectively. The GWP of the CO_2-derived ethanol route was further compared with reported 3-HP production routes based on glycerol–molasses and brewer's spent grain (**Fig. 7g**). The corresponding GWPs were 1.39, 1.71 and 9.07 kg CO_2-eq/kg 3-HP, respectively[67,68].

Discussion

Direct biological upgrading of CO_2 is intrinsically constrained by its highly oxidized state and therefore requires substantial energy and reducing power[1,69]. Here, we couple chemical CO_2 reduction with microbial 3-HP biosynthesis through ethanol. This strategy combines ethanol-mediated C2 carbon delivery with biological C1 incorporation, offering a potential redox advantage through ethanol-derived reducing equivalents. Among the candidate nexus molecules evaluated here, ethanol offered a favorable combination of carbon atom economy, biological accessibility and redox compatibility with 3-HP synthesis (**Fig. 1a**). Once assimilated by *K. phaffii*, the two-carbon backbone of ethanol is conserved in acetyl-CoA, while its sequential oxidation generates NADH that can support respiratory energy metabolism and the cofactor demand associated with 3-HP biosynthesis. ACC1-dependent carboxylation then introduces an additional inorganic carbon into acetyl-CoA to generate the C3 intermediate malonyl-CoA[11], establishing a chemically intuitive "2 + 1=3" carbon-convergent route. Importantly, our ^{13}C-tracing

experiments further showed that the C3 skeleton of 3-HP derives from an ethanol-derived C2 unit together with an ACC1-incorporated inorganic carbon (**Fig. 6e**). The substantial M+3 labelling observed with [U-$^{13}C_2$] ethanol in the absence of exogenous bicarbonate is consistent with recycling of ethanol-derived CO_2 through the carboxylation step (**Fig. 6e**), which may contribute to the high 3-HP titer achieved without bicarbonate supplementation or CO_2 sparging (**Fig. 6a and Extended Data Fig. 6a**). Conversely, supplementation with $NaHCO_3$ increased the 3-HP titer during fed-batch fermentation (**Extended Data Fig. 7a, b**), indicating that ethanol-driven biosynthesis can also benefit from an external inorganic-carbon supply. Together, these complementary observations support a carbon-convergent process in which ethanol provides the reduced C2 precursor, while inorganic carbon, generated through ethanol metabolism or supplied exogenously, contributes the additional C1 unit required for 3-HP formation.

The efficient ethanol-to-3-HP conversion required system-level reprogramming of carbon, redox and energy metabolism[70,71]. This principle was already apparent during strain construction: reinforcing ethanol oxidation enhanced ethanol assimilation and 3-HP formation, particularly under high ethanol loading, but this benefit depended on sufficient acetate activation and downstream pathway capacity. Efficient conversion therefore required coordinated engineering of ACS1 together with ACC1-, MCR- and cofactor-associated modules, thereby coupling increased upstream carbon supply to productive downstream flux (**Fig. 5a**). The resulting strain LT-28 phenotype therefore reflects a dynamically balanced high-flux state rather than simple overproduction of acetyl-CoA (**Fig. 5b, d-g, Fig. 6f, g and Extended Data Fig. 6h, i**). This interpretation is further supported by the extensive metabolic reprogramming observed in the final strain, including changes in the glyoxylate cycle, TCA cycle, gluconeogenesis, oxidative phosphorylation, redox cofactors and adenylate energy charge. These adaptations are particularly relevant for growth on ethanol because acetyl-CoA must simultaneously support product synthesis, respiration and the glyoxylate-cycle-dependent generation of biosynthetic carbon skeletons; excessive redirection of this central node towards 3-HP would therefore compromise the very growth and energy-generating functions required to sustain production. The membrane phenotype points to the same systems-level constraint. Although malonyl-CoA is also the precursor for fatty-acid synthesis, we deliberately retained endogenous lipid metabolism (**Fig. 5a**), and the downregulation of FAS1/FAS2 together with increased glycerol-3-phosphate suggests that LT-28 adapted not by simply increasing bulk fatty-acid synthesis but by reorganizing membrane-lipid metabolism (**Fig.6e and Extended Data Fig. 8a-c**). Alcohol exposure is known to perturb membrane organization and permeability, with longer-chain alcohols generally imposing greater membrane stress than ethanol, emphasizing the importance of maintaining membrane homeostasis during alcohol-based fermentation[27,30,72,73]. The high biomass density, sustained viability under pH-controlled fermentation and record de novo 3-HP titer therefore result from coordinated allocation among carbon assimilation, redox balancing, energy generation and stress adaptation[74].

The remaining challenge lies increasingly at the chemical–biological interface rather than

within either module alone. Direct feeding of the thermocatalytic liquid demonstrated that extensive purification is not intrinsically required for CO_2-to-3-HP conversion (**Fig. 7b and Extended Data Fig. 9a, d**). Current CO_2-to-ethanol catalysis still faces coupled challenges in CO_2 conversion, C–C coupling, ethanol selectivity and catalyst stability, and advances in catalyst composition, promoters, supports and tandem reaction architectures provide routes for increasing ethanol productivity and selectivity[3,12,21,75,76]. Increasing the ethanol concentration of the thermocatalytic stream would reduce the liquid volume required by the biological module and should therefore become a major target for future catalyst and reactor development. Equally important is the suppression of longer-chain alcohol coproducts, such as propanol and butanol detected in the thermocatalytic mixture. Compared with ethanol, these longer-chain alcohols partition more readily into lipid bilayers and can impose stronger membrane stress, with butanol being particularly disruptive because of its greater hydrophobicity[30,72]. This constraint highlights two complementary routes for further optimization: improving catalyst selectivity to minimize inhibitory alcohol coproducts, and increasing microbial tolerance to complex thermocatalytic effluents through adaptive evolution (ALE) or targeted stress-response engineering[29].

The integration of TEA and LCA highlights the potential of coupling thermocatalytic CO_2 upgrading with microbial synthesis for low-carbon biomanufacturing. At an annual capacity of 5,000 t 3-HP, the process corresponds to a gross utilization of approximately 49,950 t CO_2/year, while achieving an MSP of US$1.07/kg and a cradle-to-gate GWP of 1.39 kg CO_2-eq/kg 3-HP (**Fig. 7c-g and Supplementary Table 16.**). The analysis further identifies low-carbon H_2 supply, CO_2 utilization and SCP valorization as key determinants of process sustainability. Rather than relying solely on biological carbon fixation, this hybrid strategy converts CO_2 into a readily assimilable C2 intermediate and subsequently channels it into microbial 3-HP synthesis. Such a chemical–biological integration provides a scalable approach for carbon-efficient manufacturing and, with further reductions in H_2-related emissions and improved co-product utilization, may offer a route towards carbon-negative biomanufacturing.

Methods

Strains and plasmids

All the strains used in this study are detailed in **Supplementary Table 1**. The yeast strains *K. phaffii GS115*, *Y. lipolytica* PO1f, *R. toruloides* NP11, *S. cerevisiae* BY4741, *O. polymorpha* NCYC495, and *S. cerevisiae* CEN.PK2-1C were obtained from Invitrogen and Wuhan Huizao Biotechnology Co., Ltd. In this study, GS115 (Invitrogen) was used as the background strain for the production of 3-HP.

E. coli DH5α strains were used for plasmid construction. *E. coli* BL21(DE3) strains were used for the expression of recombinant proteins. PCR amplification and overlap were performed using PrimeSTAR Max DNA Polymerase (TaKaRa). All plasmids in this study

were cloned using the Gibson assembly method[77]. DNA gel purification and plasmid extraction kits were purchased from Omega. The main plasmids used in this study are listed in **Supplementary Table 2**.

Gene editing and manipulation

Gene knockout and gene insertion in GS115 were generated using a CRISPR–Cas9 system[78]. For *Cas9* insertion, HHP-sgRNA-His4 plasmid together with linearized plasmid pPIC9K-His-GAPp-Cas9-AOX1t (donor DNA) were introduced into electrocompetent GS115 cells by electroporation (Gene Pulser Xcell, Bio-Rad). Genes were integrated into the GS115 genome by homologous recombination. For other gene insertion, used the HHP-sgRNA plasmids corresponding to the specific site, and the linearized donor plasmid containing 500-1000 bp upstream and downstream homology arms. For gene knockout, the donor DNA was obtained from the overlapping region of the 1000 bp homologous arms upstream and downstream of the target gene.

All the plasmids used in this study are detailed in **Supplementary Table 2**. The main primers used in this study are detailed in **Supplementary Table 3**. All the genes overexpressed or knocked out used in this study are detailed in **Supplementary Table 4**. All the synthesized gene sequences are detailed in **Supplementary Table 5**. All the SgRNA sequences and genomic integration sites used in this study are detailed in **Supplementary Table 6**.

Strain cultivation and selection

All *E. coli* strains used for plasmid propagation were cultivated overnight in Lysogeny Broth (LB) medium at 37°C with shaking at 220 rpm. LB medium was composed of 10 g/L tryptone (Sangon Biotech), 5 g/L yeast extract (Oxoid) and 10 g/L NaCl (Sangon Biotech). LB agar medium was LB supplemented with 20 g/L agar (Sangon Biotech). Suitable 100 mg/L ampicillin (Sangon Biotech) was added for plasmid selection.

Transformed yeast cells were selected on YPD agar plates (10 g/L yeast extract, 20 g/L peptone (Sangon Biotech), 20 g/L glucose (Sangon Biotech) and 20 g/L agar) supplemented with Hygromycin B (200 mg/L). Positive colonies were verified by colony PCR using KOD FX Polymerase (Toyobo).

Shake-flask fermentation

For shake-flask fermentation, the yeast strains were initially activated on a solid YPD plate, then transferred to liquid YPD for a second activation, harvested, washed twice with sterile water, and finally transferred into 50 mL of YNE medium (13.4 g/L YNB (BD), 1.31g/L amino acids supplement (Coolaber)) containing ethanol at a defined concentration in 250 mL shake flask, with an initial OD_{600} of 0.2. The cultures were incubated at 30°C and 220 rpm. Then incubated for 72-120 h to measuring the 3-HP titer by HPLC. Cell growth was

monitored by measuring OD_{600} (MAPADA).

For fed-batch shake-flask fermentation, the yeast strains were initially activated on a solid YPD plate, then transferred to liquid YPD for a second activation, harvested, washed twice with sterile water, and finally transferred into 50 mL of YNE medium containing 10 g/L ethanol in 250 mL shake flask, with an initial OD_{600} of 0.2. Intermittent pulse feeding of pure ethanol (0.2–0.5 mL) paired with an equal volume of 2.5×YNB (33.5 g/L YNB) solution was initiated at 48 h and maintained every 24–48 h. The cultures were incubated at 30°C and 220 rpm and fermentation was terminated at 160 h. Cell growth was monitored by measuring OD_{600} and the 3-HP titer was determined by HPLC.

For shake-flask fermentation of evaluating the six yeast strains, the strains were initially activated on solid YPD plates, then transferred to liquid YPD for a second activation, harvested, washed twice with sterile water, and finally transferred into 50 mL of YNE medium (6.7 g/L YNB, 1.31 g/L amino acids supplement) containing 10 g/L ethanol or 50 mL of YNA medium (6.7 g/L YNB, 1.31 g/L amino acids supplement) containing 3 g/L acetic acid in 250 mL shake flasks with an initial OD_{600} of 0.2. The cultures were incubated at 30 °C and 220 rpm. Sampling was initiated at 12 h, and cell growth was monitored by measuring OD_{600}, while ethanol and acetate concentrations were determined by HPLC.

Fed-Batch Fermentation in Bioreactor

The engineered strain LT-28 was selected for fed-batch fermentation. LT-28 was initially activated on solid YPD plates, then transferred to liquid YPD for a second activation, harvested, washed twice with sterile water, and finally transferred into 50 mL of YNE medium containing 10 g/L ethanol in 250 mL shake flask, with an initial OD_{600} of 0.2. Incubated at 30 °C and 220 rpm for 30–36 h to obtain the seed culture. Then, the seed culture was inoculated into bioreactor (Initial OD_{600}=0.8) for fed-batch fermentation at 30 °C.

Fed-batch fermentation was performed in a 1 L DasGip bioreactor system (Eppendorf) containing 300 mL optimized Verduyn medium supplemented with 8 g/L ethanol and 800 µL of 0.5×defoamer (Sigma). The temperature, agitation, aeration, and pH were monitored and controlled using a DasGip Control 4.0 System. The temperature was kept at 30 °C, and the initial agitation was set to 400 rpm and increased to maximally 1100 rpm depending on the dissolved oxygen (DO) level. Aeration was initially set as 6 sL/h and increased to maximally 60 sL/h depending on the DO level. The dissolved oxygen level was maintained above 30%. Ethanol feeding was controlled by a DO-responsive strategy: when DO exceeded 40%, pure ethanol was fed at 8–16 mL/h, whereas ethanol feeding was stopped when DO decreased below 30%. During ethanol feeding, a salt solution was simultaneously supplied at 4–8 mL/h. The pH was kept at pH 5.6 by automatic addition of 25–28% (w/w) $NH_3{\cdot}H2O$ and 2 M HCl.

The optimized Verduyn medium contained 15 g/L $(NH_4)_2SO_4$, 8 g/L KH_2PO_4, and 6.15 g/L

$MgSO_4 \cdot 7H_2O$, supplemented with 10 mL/L trace element solution and 12 mL/L vitamin solution. Ethanol (8 g/L) was used as the carbon source. For ethanol-containing medium, ethanol was added aseptically after autoclaving and cooling of the basal medium. The trace element solution contained 19 g/L $Na_2EDTA \cdot 2H_2O$, 10.25 g/L $ZnSO_4 \cdot 7H_2O$, 0.51 g/L $MnCl_2 \cdot 4H_2O$, 0.78 g/L $CuSO_4 \cdot 5H_2O$, 0.86 g/L $CoCl_2 \cdot 6H_2O$, 0.57 g/L $Na_2MoO_4 \cdot 2H_2O$, 2.90 g/L $CaCl_2$, and 5.15 g/L $FeSO_4 \cdot 7H_2O$. The solution was sterilized by filtration through a 0.22-μm membrane. The vitamin solution contained 0.05 g/L D-biotin, 1 g/L calcium pantothenate, 1 g/L nicotinic acid, 25 g/L myo-inositol, 1 g/L thiamine hydrochloride, 1 g/L pyridoxine hydrochloride, and 0.2 g/L 4-aminobenzoic acid. The solution was filter-sterilized through a 0.22-μm membrane and protected from light. The feeding salt solution contained 9 g/L of KH_2PO_4, 5.12 g/L of $MgSO_4 \cdot 7H_2O$, 3.5 g/L K_2SO_4, 0.28 g/L Na_2SO_4. The chemicals and reagents used for preparation of the above media were obtained from Sigma-Aldrich, Aladdin, and Sangon Biotech.

To evaluate the effect of $NaHCO_3$ supplementation on 3-HP production, fed-batch fermentation of LT-28 was performed in parallel 1 L DasGip bioreactors under the conditions described above, except that the pH was maintained at 6.8 throughout fermentation. Both bioreactors initially contained 300 mL of optimized Verduyn medium supplemented with 8 g/L ethanol. The experimental bioreactor was additionally supplemented with 50 mM $NaHCO_3$ in the initial medium and 300 mM $NaHCO_3$ in the feeding salt solution, whereas the control received no $NaHCO_3$. $MgSO_4 \cdot 7H_2O$ was omitted from the feeding salt solutions and instead supplied separately as 0.8 mL of a sterile 0.145 g/mL stock solution every 24 h, starting approximately 24 h after the initiation of feeding. Both bioreactors were operated using the same DO-responsive ethanol feeding strategy, with all other fermentation parameters maintained as described above.

For the coupled conversion of CO_2-derived thermocatalytic liquid to 3-HP, LT-28 was cultivated in the bioreactor under the same conditions described above. When the culture reached an OD_{600} of approximately 60, a portion of the culture broth was aseptically withdrawn to reduce the working volume to 110 mL. The temperature was maintained at 30 °C, the pH was controlled at 5.6, and the DO-responsive control strategy was maintained unchanged. Subsequently, 2 mL of 1 M $NaHCO_3$ was added, and the carbon feed was switched from pure ethanol to the CO_2-derived thermocatalytic liquid, which was defined as 0 h of the coupled bioconversion phase. The thermocatalytic liquid was supplied using the same DO-responsive feeding strategy described above, whereas feeding of the salt solution was discontinued at the start of the coupled bioconversion phase. A schematic illustration of the coupled thermocatalytic–biocatalytic process is shown in **Extended Data Fig. 9a**.

Comparative transcriptomic analysis

To compare the metabolic characteristics of the six yeast strains, cells were first routinely activated in YPD medium and then inoculated into 50 mL of YNE medium containing 10 g/L ethanol or 50 mL of YNA medium containing 3 g/L acetic acid in 250 mL shake flasks with an initial OD_{600} of 0.2. Cultures were incubated at 30 °C and 220 rpm and harvested

at the mid-exponential growth phase. For transcriptomic analysis, 5–10 mL of culture was rapidly collected, washed twice with PBS, immediately frozen in liquid nitrogen, and stored until RNA extraction. Total RNA was extracted using TRIzol reagent (Invitrogen). RNA quality and integrity were assessed using a NanoDrop 2000 spectrophotometer (Thermo Fisher Scientific) and an Agilent 2100 Bioanalyzer (Agilent Technologies). mRNA was enriched with oligo(dT) magnetic beads, fragmented, reverse-transcribed into cDNA, and used for library construction with the Illumina TruSeq RNA Sample Preparation Kit. Sequencing was performed on an Illumina HiSeq 4000 platform.

The reference genomes used for the six yeast strains are listed in **Supplementary Table 7**. For the *S. cerevisiae* CEN.PK2-1C strain, the *S. cerevisiae* CEN.PK113-7D genome was used as the reference because the available CEN.PK2-1C assembly was highly fragmented, whereas CEN.PK113-7D provides a high-quality chromosome-level genome assembly. As both strains belong to the closely related CEN.PK lineage and show very high genome sequence similarity, CEN.PK113-7D was considered an appropriate reference for gene expression mapping and orthologous-group analysis.
Orthologous genes among the six yeast species were assigned to orthogroups (OGs) using OrthoFinder. Paralogous genes were retained to avoid loss of functionally relevant genes in species containing multiple members of the same orthogroup. For each OG, TPM values of all genes assigned to the same OG within a given species were summed to obtain the corresponding orthogroup-level expression value.

For PCA, orthogroup-level TPM values from the ethanol-grown samples were transformed as $\log_2(\text{TPM}+1)$, and PCA was performed across the six yeast strains using the resulting expression matrix. For visualization of metabolic features, 19 representative genes associated with ethanol and acetate utilization and related metabolic processes were selected based on their orthogroup assignments. Their orthogroup-level expression values were transformed as $\log_2(\text{TPM}+1)$, standardized by row-wise Z-score across the six yeast strains, and visualized as a heatmap using Python.

Proteomic analysis

Strains LT-13 and LT-28 were cultivated under the intermittent pulse-feeding conditions described above. At 48 h, 0.5 mL pure ethanol and 0.5 mL 2.5×YNB were added, and cells were collected 18 h later, when stable differences in ethanol consumption and 3-HP production had been established. Cells were washed twice with PBS, normalized to 100 OD_{600} units per sample, and immediately frozen in liquid nitrogen.

For protein extraction, frozen cell pellets were lysed in 8 M urea and 1% SDS containing protease inhibitors, homogenized, sonicated at low temperature and centrifuged to remove insoluble material. Protein concentrations were determined using a BCA assay. Proteins (30–50 μg) were reduced with 10 mM TCEP at 37 °C for 60 min, alkylated with 40 mM iodoacetamide for 40 min in the dark, precipitated with precooled acetone, and digested overnight with trypsin at 37 °C at an enzyme-to-protein ratio of 1:40. Peptides were desalted, dried, reconstituted in 0.1% formic acid and quantified before liquid

chromatography–mass spectrometry (LC–MS)/MS analysis.

Peptides were separated on a Vanquish Neo nano-LC system (Thermo Fisher Scientific) using a homemade C18 column (15 cm×100 μm, 1.7 μm). Mass spectrometric analysis was performed on an Orbitrap Astral mass spectrometer (Thermo Fisher Scientific) in data-independent acquisition (DIA) mode with positive-ion detection. The ion-source voltage was set to 1.8 kV, with MS1 and MS2 scan ranges of m/z 380–980 and 150–2,000, respectively. Data were acquired using Thermo Xcalibur 4.7. Differential protein abundance between LT-28 and LT-13 was evaluated using an unpaired two-sided Student's t-test, with *P* values adjusted by the Benjamini–Hochberg (BH) method. Proteins with FC > 1.2 or < 0.83 and $P<0.05$ were considered significantly up- or downregulated, respectively. Volcano plots were generated in Python using $\log_2$FC and $-\log_{10}$(*P*. adj), where FC is fold change.

Metabolite and metabolomic analysis

Targeted metabolomic analysis was performed using the same biological sampling procedure as described for proteomic analysis and focused on central carbon and energy metabolism. For central-carbon metabolite profiling, approximately 10 mg of cell biomass was extracted with isotope-labelled internal standards, 50% aqueous methanol and acetonitrile. After centrifugation, the supernatant was derivatized with 3-nitrophenylhydrazine hydrochloride (3NPH·HCl) and EDC·HCl at 60 °C for 40 min. Metabolites were analysed by LC–ESI–MS/MS using an ExionLC AD system coupled to a QTRAP 6500+ mass spectrometer (SCIEX) and a Waters HSS T3 column (2.1×150 mm, 1.8 μm). Chromatographic separation was performed at 40 °C and 0.4 mL/min using 0.03% formic acid in water and 0.03% formic acid in acetonitrile as mobile phases, with electrospray ionization operated in both positive and negative modes.

For energy-metabolism profiling, approximately 20 mg of cell biomass was extracted with 80% aqueous methanol, followed by cryogenic grinding, sonication and centrifugation. The supernatant was dried under nitrogen and reconstituted in 50% aqueous acetonitrile containing internal standards. Metabolites were analysed using an ExionLC AD system coupled to a QTRAP 7500 mass spectrometer (SCIEX) with a BEH HILIC column (4.6×250 mm, 5 μm) at 40 °C, using 15 mM ammonium bicarbonate containing 0.4% aqueous ammonia and acetonitrile as mobile phases. Negative-mode electrospray ionization was used for MS/MS detection.

Differences in metabolite abundance between LT-28 and LT-13 were assessed using an unpaired two-sided Student's t-test, with BH correction for multiple comparisons. Metabolites with $P<0.05$ were considered significantly altered, with FC>1 and FC<1 indicating increased and decreased abundance, respectively. KEGG pathway enrichment analysis was performed using the KEGG database (KEGG_V20230830), and enrichment P values were corrected using the BH method. Pathway enrichment results were visualized in Python using $-\log_{10}$(*P*. adj).

DCW determination

DCW was determined gravimetrically. A defined volume of yeast culture was collected and centrifuged to harvest the cells. The cell pellet was washed twice with deionized water to remove residual medium components and then dried at 80–105 °C until a constant weight was reached. DCW was calculated from the difference between the weight of the dried cell-containing tube and that of the pre-weighed empty tube, and expressed as g/L culture. For bioreactor cultivations, samples were collected directly at the indicated fermentation time points, and DCW was determined independently rather than estimated from shake-flask OD_{600}–DCW calibration curves. For comparison among different yeast species, OD_{600} and DCW were measured over a series of culture dilutions to establish strain-specific OD_{600}–DCW calibration curves.

Molecular dynamics simulations

Molecular dynamics (MD) simulations were performed to compare the accessibility of K626 to acetyl-CoA in *K. phaffii* ACS1wt and the ACS1-I658P variant. Each simulation system contained ACS1, a truncated GNAT acetyltransferase domain (PDB ID: 4U5Y) and one acetyl-CoA molecule. Structural models of ACS1wt and ACS1-I658P were generated using AlphaFold, with the *S. cerevisiae* ACS structure (PDB ID: 1RY2) used as a structural reference. For each variant, eight independent 500 ns MD simulations were performed. All system preparation, equilibration and production simulations were performed using Amber 24, and trajectory analyses were carried out using CPPTRAJ (AmberTools v6.24.0).

Proteins were described using the ff14SB force field, and acetyl-CoA was parameterized using GAFF2 with AM1-BCC atomic charges. The complexes were solvated in TIP3P water, charge-neutralized with sodium ions, and supplemented with NaCl. Long-range electrostatic interactions were treated using particle-mesh Ewald, with a 10 Å cutoff. Bonds involving hydrogen atoms were constrained using SHAKE with a 2 fs integration time step. Following energy minimization, the systems were heated to 300 K and equilibrated under NVT and NPT conditions. Production simulations were performed at 300 K and 1.0 bar. Trajectories were saved every 10 ps, and every tenth frame was used for subsequent analysis.

The accessibility of K626 for acetyl transfer was evaluated using geometric descriptors between the terminal side-chain nitrogen of K626 (NZ) and the acetyl carbonyl group of acetyl-CoA. The NZ–C distance was defined as the distance between K626 NZ and the acetyl carbonyl carbon (C) of acetyl-CoA, and a short-contact geometry was defined by an NZ–C distance <4.5 Å. An acetylation-compatible near-attack geometry was defined by the simultaneous occurrence of an NZ–C distance <4.5 Å and an NZ–C–O angle of 90–120°, with O representing the carbonyl oxygen of acetyl-CoA. The NZ–C–O angle was defined by K626 NZ, the acetyl carbonyl carbon and the corresponding carbonyl oxygen. K626 orientation relative to acetyl-CoA was further evaluated using the CE–NZ–C angle, defined by the K626 CE atom, K626 NZ and the acetyl carbonyl carbon; angles of 90–150° were classified as a toward-acetyl-CoA orientation.

Enzyme activity assay

K. phaffii ACS1wt and ACS1-I658P were expressed in recombinant *E. coli* BL21(DE3) strains LT-23 and LT-24, respectively. Protein expression was induced with 0.2 mM IPTG at 16 °C for 18 h, and the proteins were purified by Ni-affinity chromatography using an ÄKTA system (Cytiva). Enzyme activity was assayed in 500 µL reaction mixtures containing 0.2 µM purified ACS1, 2 mM ATP, 1 mM CoA, 0.1 mM DTT, 5 mM $MgCl_2$ and 0.01–5 mM acetate in HEPES buffer (pH 7.5). The chemicals and reagents used for preparation of the above media were obtained from Sigma-Aldrich and Sangon Biotech. Reactions were performed at 30 °C for 10 min and terminated by adding an equal volume of acetonitrile. Acetyl-CoA formation was quantified by LC–MS (Waters). Kinetic parameters were obtained by nonlinear fitting to the Michaelis–Menten equation using GraphPad Prism.

SEM observation

For scanning electron microscopy (SEM), fermentation samples collected at 0, 85 and 157 h were harvested, washed with PBS and fixed overnight at 4 °C in 2% paraformaldehyde and 2.5% glutaraldehyde. Cells were post-fixed with 1% osmium tetroxide, dehydrated through a graded ethanol series, and subjected to critical-point drying using a Leica EM CPD300. Dried samples were sputter-coated with a 6 nm Pt layer using a Leica EM ACE600 and examined by SEM at 5,000× magnification and an accelerating voltage of 3 kV using a secondary electron detector.

PI staining

Yeast cells were harvested during the exponential phase, washed with PBS and stained with PI (Invitrogen) at a final concentration of 2 µg/mL for 8 min at room temperature in the dark. Cells were imaged using a Zeiss LSM900 confocal microscope equipped with an Airyscan 2 detector and a 63× oil-immersion objective. PI fluorescence was recorded in the red channel (Ex 561 nm, Em 617 nm), and cells were segmented from transmitted-light images. The same regions of interest were applied to the fluorescence images, and PI-positive cells were quantified in ImageJ as the percentage of cells exhibiting red fluorescence. At least five randomly selected fields were analysed per sample.

Analytical methods

Cell density was measured at 600 nm using a spectrophotometer (Shimadzu). Ethanol, acetate, and 3-HP concentrations were determined by high-performance liquid chromatography (HPLC) using an Agilent 1260 Infinity III system equipped with an Aminex HPX-87H column (Bio-Rad) and a refractive index detector (RID). Before analysis, all samples were filtered through a 0.22 µm aqueous membrane filter. The HPLC analysis was performed using 5.00 mM H_2SO_4 as the mobile phase at a flow rate of 0.6 mL/min, with the column temperature maintained at 65 °C. Ethanol, acetate, propanol, and propionate in the liquid products obtained from CO_2 thermocatalysis were quantified using the same HPLC method. Butanol in the liquid products obtained from CO_2 thermocatalysis was quantified by gas chromatography (GC) using an Agilent 8890 GC

system equipped with a flame ionization detector (FID). Separation was achieved on an HP-FFAP capillary column (Agilent) using N_2 as the carrier gas at 2.25 mL/min. The injector and detector temperatures were maintained at 210 °C and 230 °C, respectively. The oven temperature was held at 70 °C for 2 min, increased to 200 °C at 50 °C/min, and held for 1 min.

CO_2 thermocatalysis

The performance evaluation for CO_2 hydrogenation to ethanol was performed in a high-pressure fixed-bed continuous-flow reactor. A dual-bed catalyst configuration was employed: 300 mg of KNiCuFe catalyst was packed as the upper layer, and 600 mg of Cu/ZnO/Al_2O_3 catalyst was packed as the lower layer, with the two catalytic components separated by quartz wool.

Prior to the catalytic measurements, the catalyst bed was pretreated in a mixed gas of 5 mL/min CO and 45 mL/min Ar at 350 °C for 5 h under atmospheric pressure for activation. Then, the activation gas was switched to pure Ar, and the temperature was cooled to 320 °C. Three different feed-gas compositions were evaluated for CO_2 thermocatalysis. Gas mixture 1 consisted of 24% CO_2, 72% H_2 and 4% Ar (CO-free), whereas gas mixture 2 contained 18% CO_2, 8% CO, 70% H_2 and 4% Ar (vol%). In addition, an Industrial off-gas containing approximately 36% H_2, 37% CO and 25% CO_2 was evaluated as a practical feedstock. After condensation and collection, the liquid products were analyzed by Agilent HPLC and GC.

^{13}C isotope tracing of carbon incorporation into 3-HP

For ^{13}C isotope-tracing experiments, strain LT-28 was first activated on YPD agar plates and subsequently cultivated in YNE medium containing 10 g/L ethanol for 36–48 h. The OD_{600} was measured, and cells corresponding to 150 OD_{600} units were collected by centrifugation and washed twice with sterile water. The harvested cells were resuspended in 5 mL of 50 mM potassium phosphate (KPi) buffer and starved for 12 h to minimize interference from residual intracellular carbon pools. After starvation, the cells were collected by centrifugation, washed once with sterile water and resuspended in fresh 50 mM KPi buffer.

Six isotope-labeling conditions were established using unlabeled or uniformly ^{13}C-labelled ethanol ([U-$^{13}C_2$] ethanol), with or without unlabeled or ^{13}C-labelled Na$H^{13}CO_3$, as detailed in **Supplementary Table 9**. Each reaction contained cells corresponding to 150 OD_{600} units in a final volume of 5 ml. Where indicated, ethanol and $NaHCO_3$ were supplied at final concentrations of 100 mM and 30 mM, respectively. Reactions were carried out in serum bottles at 25 °C and 200 rpm, and samples were collected at 6 h intervals. After centrifugation, the supernatants were analysed by LC – MS (Waters). The mass isotopologue distributions of 3-HP, including M+0, M+1, M+2 and M+3, were determined to evaluate carbon incorporation from ethanol and inorganic carbon.

Statistical analyses

Two-sided unpaired Welch's t-tests were used for comparisons between two groups. For comparisons involving more than two groups, one-way analysis of variance (ANOVA) followed by Dunnett's multiple-comparisons test was used. Unless stated otherwise in the figure legends, data are shown as mean ± s.d. with n=3 biologically independent samples per condition.

Data availability

All data supporting the findings of this study are included in this article and its Supplementary Information. Source data are provided with this paper.

References

1 Nielsen, D. U., Hu, X.-M., Daasbjerg, K. & Skrydstrup, T. Chemically and electrochemically catalysed conversion of CO_2 to CO with follow-up utilization to value-added chemicals. *Nature Catalysis*. **1**, 244-254 (2018)

2 Gao, D., Arán-Ais, R. M., Jeon, H. S. & Roldan Cuenya, B. Rational catalyst and electrolyte design for CO_2 electroreduction towards multicarbon products. *Nature Catalysis*. **2**, 198-210 (2019)

3 Moon, H. S., Jaffer, S. A., Miao, R. K., Sargent, E. H. & Sinton, D. Scaling electrocatalysts for reduction of CO_2 or CO to multicarbon products. *Nature Reviews Materials*. **11**, 244-254 (2026)

4 Shafaat, H. S. & Yang, J. Y. Uniting biological and chemical strategies for selective CO_2 reduction. *Nature Catalysis*. **4**, 928-933 (2021)

5 Liu, Q., Wu, L., Jackstell, R. & Beller, M. Using carbon dioxide as a building block in organic synthesis. *Nature Communications*. **6**, 5933 (2015)

6 Zhou, G. et al. Bioadaptive Ni single atoms unlock high rate microbial electrosynthesis of isopropanol from CO_2. *Nature Communications*. **17**, 1639 (2026)

7 Guan, X., Xie, Y. & Liu, C. Performance evaluation and multidisciplinary analysis of catalytic fixation reactions by material–microbe hybrids. *Nature Catalysis*. **7**, 475-482 (2024)

8 Cestellos-Blanco, S., Zhang, H., Kim, J. M., Shen, Y.-x. & Yang, P. Photosynthetic semiconductor biohybrids for solar-driven biocatalysis. *Nature Catalysis*. **3**, 245-255 (2020)

9 Jones, S. W. et al. CO_2 fixation by anaerobic non-photosynthetic mixotrophy for improved carbon conversion. *Nature Communications*. **7**, 12800 (2016)

10 Bachleitner, S., Ata, Ö. & Mattanovich, D. The potential of CO_2-based production cycles in biotechnology to fight the climate crisis. *Nature Communications*. **14**, 6978 (2023)

11 Qin, N. et al. Increased CO_2 fixation enables high carbon-yield production of 3-hydroxypropionic acid in yeast. *Nature Communications*. **15**, 1591 (2024)

12 Jiang, X., Nie, X., Guo, X., Song, C. & Chen, J. G. Recent advances in carbon dioxide hydrogenation to methanol via heterogeneous catalysis. *Chemical Reviews*. **120**, 7984-8034 (2020)

13 Zhang, Y. et al. Engineering yeast mitochondrial metabolism for 3-hydroxypropionate production. *Biotechnology for Biofuels and Bioproducts*. **16**, 64 (2023)

14 Kang, F. et al. Expanding the genetic toolkit of *Yarrowia lipolytica*: Dynamic promoter engineering enables high-titer biosynthesis of 3-hydroxypropionic acid. *Bioresource Technology*. **432**, 132656 (2025)

15 Chen, Z. et al. Metabolic engineering of *Corynebacterium glutamicum* for the production of 3-hydroxypropionic acid from glucose and xylose. *Metabolic Engineering*. **39**, 151-158 (2017)

16 Zhang, Y. et al. High-level co-production of 3-hydroxypropionic acid and 1,3-propanediol from glycerol: Metabolic engineering and process optimization. *Bioresource Technology*. **369**, 128438 (2023)

17 Cao, Q.-Y., Xu, H.-Y., Ye, B.-C. & Zhou, Y. Metabolic and fermentation engineering of *Klebsiella Pneumoniae* for high-level production of 3-hydroxypropionic acid. *Archives of Microbiology*. **207**, 196 (2025)

18 Russmayer, H., Ergoth, S., Marx, H. & Sauer, M. Process engineering towards an oxidative cellular state improves 3-hydroxypropionic acid production with *Lentilactobacillus diolivorans*. *Bioresource Technology*. **382**, 129160 (2023)

19 Wang, X., Cui, Z., Sun, X., Wang, Z. & Chen, T. Production of 3-hydroxypropionic acid from renewable substrates by metabolically engineered microorganisms: A review. *Molecules* **28**, 1888 (2023).

20 Liang, B. et al. Recent advances, challenges and metabolic engineering strategies in the biosynthesis of 3-hydroxypropionic acid. *Biotechnology and Bioengineering*. **119**, 2639-2668 (2022)

21 Xiang, W. et al. NiFe2O4 spinel engineering for transcending the dilemma of activity–selectivity in CO_2 hydrogenation to ethanol. *Nature Communications*. **17**, 572 (2025)

22 Li, F. et al. Cooperative CO_2-to-ethanol conversion via enriched intermediates at molecule–metal catalyst interfaces. *Nature Catalysis*. **3**, 75-82 (2020)

23 Shayesteh Zeraati, A. et al. Carbon- and energy-efficient ethanol electrosynthesis via interfacial cation enrichment. *Nature Synthesis*. **4**, 75-83 (2025)

24 Liu, Y. et al. Engineered ethanol-driven biosynthetic system for improving production of acetyl-CoA derived drugs in Crabtree-negative yeast. *Metabolic Engineering*. **54**, 275-284 (2019)

25 Ohsawa, S., Nishida, S., Oku, M., Sakai, Y. & Yurimoto, H. Ethanol represses the expression of methanol-inducible genes via acetyl-CoA synthesis in the yeast *Komagataella phaffii*. *Sci Rep*. **8**, 18051 (2018)

26 Nielsen, J. Synthetic biology for engineering acetyl coenzyme A metabolism in yeast. *mBio*. **5**, e02153 (2014)

27 Sun, M. et al. Microbial conversion of ethanol to high-value products: Progress and challenges. *Biotechnol Biofuels Bioprod*. **17**, 115 (2024)

28 Zhang, M. et al. Deletion of acetate transporter gene *ADY2* improved tolerance of Saccharomyces cerevisiae against multiple stresses and enhanced ethanol production in the presence of acetic acid. *Bioresource Technology*. **245**, 1461-1468 (2017)
29 Lam, F. H., Ghaderi, A., Fink, G. R. & Stephanopoulos, G. Engineering alcohol tolerance in yeast. *Science*. **346**, 71-75 (2014)
30 Wang, S. et al. Membrane remodelling for increased methanol tolerance in *Komagataella phaffii*. *Nature Synthesis*. (2026)
31 Karaoglan, M., Erden-Karaoglan, F., Yilmaz, S. & Inan, M. Identification of major *ADH* genes in ethanol metabolism of *Pichia pastoris*. *Yeast*. **37**, 227-236 (2020)
32 Karaoglan, M., Karaoglan, F. E. & Inan, M. Functional analysis of alcohol dehydrogenase (*ADH*) genes in *Pichia pastoris*. *Biotechnology Letters*. **38**, 463-469 (2016)
33 Liu, C. et al. Functional balance between enzymes in malonyl-CoA pathway for 3-hydroxypropionate biosynthesis. *Metabolic Engineering*. **34**, 104-111 (2016)
34 Liu, C., Wang, Q., Xian, M., Ding, Y. & Zhao, G. Dissection of malonyl-coenzyme A reductase of *Chloroflexus aurantiacus* results in enzyme activity improvement. *PLoS One*. **8**, e75554 (2013)
35 Jogl, G. & Tong, L. Crystal structure of yeast acetyl-coenzyme A synthetase in complex with AMP. *Biochemistry*. **43**, 1425-1431 (2004)
36 Starai, V. J., Gardner, J. G. & Escalante-Semerena, J. C. Residue Leu-641 of acetyl-CoA synthetase is critical for the acetylation of residue Lys-609 by the protein acetyltransferase enzyme of *Salmonella enterica*. *Journal of Biological Chemistry*. **280**, 26200-26205 (2005)
37 Su, J. et al. Democratizing protein language model training, sharing and collaboration. *Nature Biotechnology*. (2025)
38 Chen, Y., Daviet, L., Schalk, M., Siewers, V. & Nielsen, J. Establishing a platform cell factory through engineering of yeast acetyl-CoA metabolism. *Metabolic Engineering*. **15**, 48-54 (2013)
39 Lian, J., Mishra, S. & Zhao, H. Recent advances in metabolic engineering of *Saccharomyces cerevisiae*: New tools and their applications. *Metabolic Engineering*. **50**, 85-108 (2018)
40 Fina, A., Heux, S., Albiol, J. & Ferrer, P. Combining metabolic engineering and multiplexed screening methods for 3-hydroxypropionic acid production in *Pichia pastoris*. *Front Bioeng Biotechnol*. **10**, 942304 (2022)
41 Ream, M. & Prather, K. L. J. Engineered autonomous dynamic regulation of metabolic flux. *Nature Reviews Bioengineering*. **2**, 233-243 (2024)
42 Bogorad, I. W., Lin, T. S. & Liao, J. C. Synthetic non-oxidative glycolysis enables complete carbon conservation. *Nature*. **502**, 693-697 (2013)
43 Pérez-Gallardo, R. V. et al. Reactive oxygen species production induced by ethanol in *Saccharomyces cerevisiae* increases because of a dysfunctional mitochondrial iron–sulfur cluster assembly system. *FEMS Yeast Research*. **13**, 804-819 (2013)
44 Kiefer, D., Merkel, M., Lilge, L., Henkel, M. & Hausmann, R. From acetate to bio-

based products: Underexploited potential for industrial biotechnology. *Trends in Biotechnology*. **39**, 397-411 (2021)

45 Jiang, W. et al. Metabolic engineering strategies to enable microbial utilization of C1 feedstocks. *Nature Chemical Biology*. **17**, 845-855 (2021)

46 Sahana, G. R. et al. A review on ethanol tolerance mechanisms in yeast: Current knowledge in biotechnological applications and future directions. *Process Biochemistry*. **138**, 1-13 (2024)

47 Covaleda-Cortés, G. et al. Bioprocess intensification for 3-hydroxypropionic acid production from methanol using engineered *Komagataella phaffii*. *Chemical Engineering Journal Advances*. **26**, 101201 (2026)

48 Wu, X. et al. Efficient bioproduction of 3-hydroxypropionic acid from methanol by a synthetic yeast cell factory. *ACS Sustainable Chemistry & Engineering*. **11**, 6445-6453 (2023)

49 Hwang, H. J., Adamczyk, P. A., Gladden, J. M. & Liu, D. Inducible flippase-mediated metabolic engineering of *Rhodosporidium toruloides* for enhanced 3-hydroxypropionic acid production from corn stover hydrolysate. *Bioresource Technology*. **439**, 133368 (2026)

50 Tan, S.-I. et al. High yield production of 3-hydroxypropionic acid using *Issatchenkia orientalis*. *Nature Communications*. **17**, 899 (2026)

51 Gao, J. et al. Engineering co-utilization of glucose and xylose for chemical overproduction from lignocellulose. *Nature Chemical Biology*. **19**, 1524-1531 (2023)

52 Hartner, F. S. & Glieder, A. Regulation of methanol utilisation pathway genes in yeasts. *Microbial Cell Factories*. **5**, 39 (2006)

53 Udom, N., Chansongkrow, P., Charoensawan, V. & Auesukaree, C. Coordination of the cell wall integrity and high-osmolarity glycerol pathways in response to ethanol stress in *Saccharomyces cerevisiae*. *Applied and Environmental Microbiology*. **85**, e00551-00519 (2019)

54 Strand, M. K. et al. POS5 gene of *Saccharomyces cerevisiae* encodes a mitochondrial NADH kinase required for stability of mitochondrial DNA. *Eukaryotic Cell*. **2**, 809-820 (2003)

55 Chen, K. et al. Electro-biodiesel empowered by co-design of microorganism and electrocatalysis. *Joule*. **9**, (2025)

56 Zheng, T. et al. Upcycling CO_2 into energy-rich long-chain compounds via electrochemical and metabolic engineering. *Nature Catalysis*. **5**, 388-396 (2022)

57 Hann, E. C. et al. A hybrid inorganic–biological artificial photosynthesis system for energy-efficient food production. *Nature Food*. **3**, 461-471 (2022)

58 Zhang, P. et al. Chem-bio interface design for rapid conversion of CO_2 to bioplastics in an integrated system. *Chem*. **8**, 3363-3381 (2022)

59 Fan, L. et al. Blended nexus molecules promote CO_2 to L-tyrosine conversion. *Science Advances*. **10**, eado1352 (2024)

60 Lim, J., Choi, S. Y., Lee, J. W., Lee, S. Y. & Lee, H. Biohybrid CO_2 electrolysis for the direct synthesis of polyesters from CO_2. *Proceedings of the National Academy of Sciences*. **120**, e2221438120 (2023)

61 Wi, T.-U. et al. Upgrading carbon monoxide to bioplastics via integrated electrochemical reduction and biosynthesis. *Nature Synthesis*. **3**, 1392-1403 (2024)
62 Guo, S. et al. Scalable electro-biosynthesis of ectoine from greenhouse gases. *Angewandte Chemie International Edition*. **64**, e202415445 (2025)
63 Fei, Q. et al. Biological valorization of natural gas for the production of lactic acid: Techno-economic analysis and life cycle assessment. *Biochemical Engineering Journal*. **158**, 107500 (2020)
64 Liu, G., Sun, J., Zhang, J., Tu, Y. & Bao, J. High titer l-lactic acid production from corn stover with minimum wastewater generation and techno-economic evaluation based on Aspen plus modeling. *Bioresource Technology*. **198**, 803-810 (2015)
65 Yu, W. et al. Methanol biotransformation for the production of biodegradable plastic monomer L-lactate in yeast. *Nature Communications*. **16**, 10756 (2025)
66 Mahata, C., Mishra, S. & Singh, V. 3-Hydroxypropionic acid recovery from fermentation broth through novel downstream processing: Technoeconomic analysis. *Bioresource Technology*. **445**, 134094 (2026)
67 Okoli, K., Dubey, P. & Mba Wright, M. Integrated techno-economic and life cycle assessment of 3-hydroxypropionic acid bioproduction from a glycerol-molasses blend. *Bioresource Technology*. **460**, 135400 (2026)
68 Kwan, T. H., Hu, Y. & Lin, C. S. K. Techno-economic analysis of a food waste valorisation process for lactic acid, lactide and poly(lactic acid) production. *Journal of Cleaner Production*. **181**, 72-87 (2018)
69 Grim, R. G. et al. The chemistry of CO_2 conversion: A review. *Chemical Reviews*. **126**, 5028-5082 (2026)
70 Lei, C. et al. Regulating the metabolic flux of pyruvate dehydrogenase bypass to enhance lipid production in *Saccharomyces cerevisiae*. *Communications Biology*. **7**, 1399 (2024)
71 Sha, Y. et al. Advances in metabolic engineering for enhanced acetyl-CoA availability in yeast. *Critical Reviews in Biotechnology*. **45**, 904-922 (2025)
72 Huffer, S., Clark Melinda, E., Ning Jonathan, C., Blanch Harvey, W. & Clark Douglas, S. Role of alcohols in growth, lipid composition, and membrane fluidity of yeasts, bacteria, and archaea. *Applied and Environmental Microbiology*. **77**, 6400-6408 (2011)
73 Liu, H. et al. Enhancing biofuels production by engineering the actin cytoskeleton in *Saccharomyces cerevisiae*. *Nature Communications*. **13**, 1886 (2022)
74 Schulz-Mirbach, H. et al. New-to-nature CO_2-dependent acetyl-CoA assimilation enabled by an engineered B12-dependent acyl-CoA mutase. *Nature Communications*. **15**, 10235 (2024)
75 Zhao, H., Zeng, C. & Tsubaki, N. A mini review on recent advances in thermocatalytic hydrogenation of carbon dioxide to value-added chemicals and fuels. *Resources Chemicals and Materials*. **1**, 230-248 (2022)
76 Kostyniuk, A. & Likozar, B. State-of-the-art advancements in the thermocatalytic conversion of CO_2 into ethanol and higher alcohols: recent progress in catalyst

development and reaction mechanisms. *Chemical Engineering Journal*. **503**, 158467 (2025)

77 Gibson, D. G. et al. Enzymatic assembly of DNA molecules up to several hundred kilobases. *Nature Methods*. **6**, 343-345 (2009)

78 Gao, J. et al. Synthetic biology toolkit for marker-less integration of multigene pathways into *Pichia pastoris* via CRISPR/Cas9. *ACS Synthetic Biology*. **11**, 623-633 (2022)

Acknowledgements

This work was financially supported by the National Key R&D Program of China (2023YFA0914000), Zhejiang Key Laboratories Project (2024E10053), Pioneer" and "Leading Goose" R&D Program of Zhejiang (2025C01094).

Author contributions

Z.A. and J.L. supervised this project, reviewed and edited the manuscript. T.L. conceived and designed the study, performed the experiments and data processing, analysed the data and wrote the manuscript. H.L. assisted with CO_2 thermocatalysis and catalyst characterization, and with fed-batch fermentation in bioreactors. Z.C. assisted with fed-batch fermentation in bioreactors, PI staining and quantification, and SEM. Y.Z. assisted with molecular dynamics simulations related to ACS1. Y.M. assisted with ^{13}C isotope-tracing experiments and extracellular carbohydrate characterization. J.F. assisted with the LCA and TEA of 3-HP production using CO_2-derived ethanol.

Competing interests

The authors declare no competing interests.

a

Nexus molecule	Assimilation pathway	Atom economy	Steps (to Acetyl-CoA)	Electron equivalents (e^- eq.)	Net reducing equivalents (NAD(P)H equivalents)	NADH/NADPH balance to 3-HP	Biocompatibility
Formate	rGly pathway → Acetyl-CoA	★★	~8	2	(-2)	Deficit	Low
Methanol	MDH → RuMP cycle → Acetyl-CoA	★★	~10	6	(+3)	Surplus	Moderate
Methane	MMO → MDH → RuMP cycle → Acetyl-CoA	★★	~11	8	(0)	Deficit	Low
Ethylene	/	/	/	12	/	/	Low
Acetate	ACS → Acetyl-CoA	★★★★★	~1	8	(0)	Deficit	High
Ethanol	ADH → ALD → ACS → Acetyl-CoA	★★★★★	~3	12	(+2)	Well balanced	High

Assimilation pathway
Acetyl-CoA — Outlines the typical assimilation pathway

Atom economy
★★★★★ Very high; ★★★★ High; ★★★ Moderate; ★★ Low

Net reducing equivalents
Positive (generates reducing power)
Neutral
Negative (requires reducing power)

NADH/NADPH balance to 3-HP (~2 NADPH required)
Well balanced — Reducing power is well matched to the requirement
Surplus — Reducing power exceeds the requirement
Deficit — Reducing power is insufficient

b

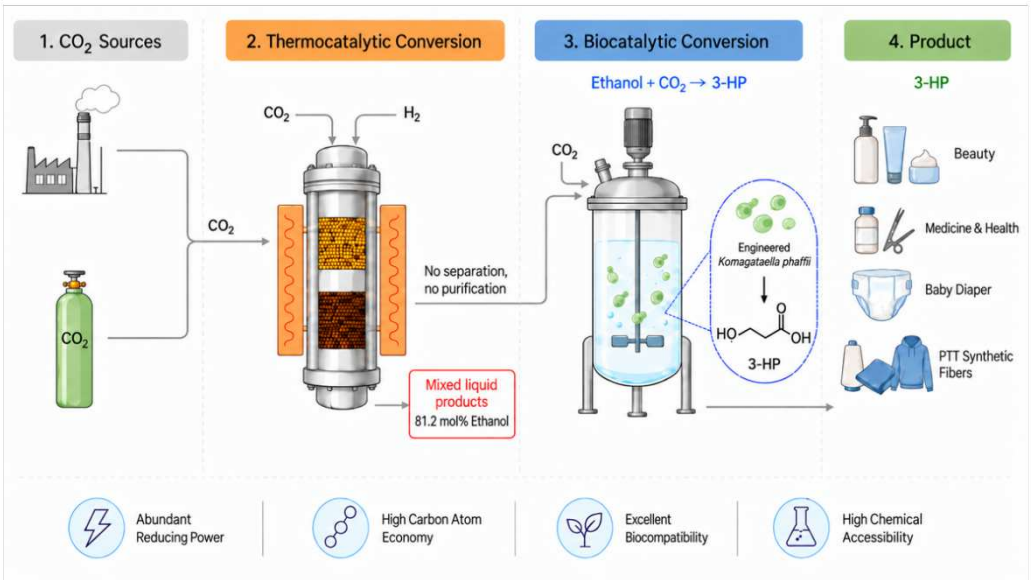

Fig. 1 | Ethanol as a nexus molecular for integrating CO_2 chemocatalysis and microbial biosynthesis. (a) Comparison of representative low-carbon products accessible from CO_2 chemocatalysis as potential intermediates for downstream biocatalysis. Definitions and evaluation criteria are provided in Supplementary Table 17. **(b)** Schematic design of the integrated CO_2-to-3-HP platform, in which thermocatalytic CO_2 reduction first produces ethanol, followed by yeast-mediated conversion of ethanol to 3-HP.

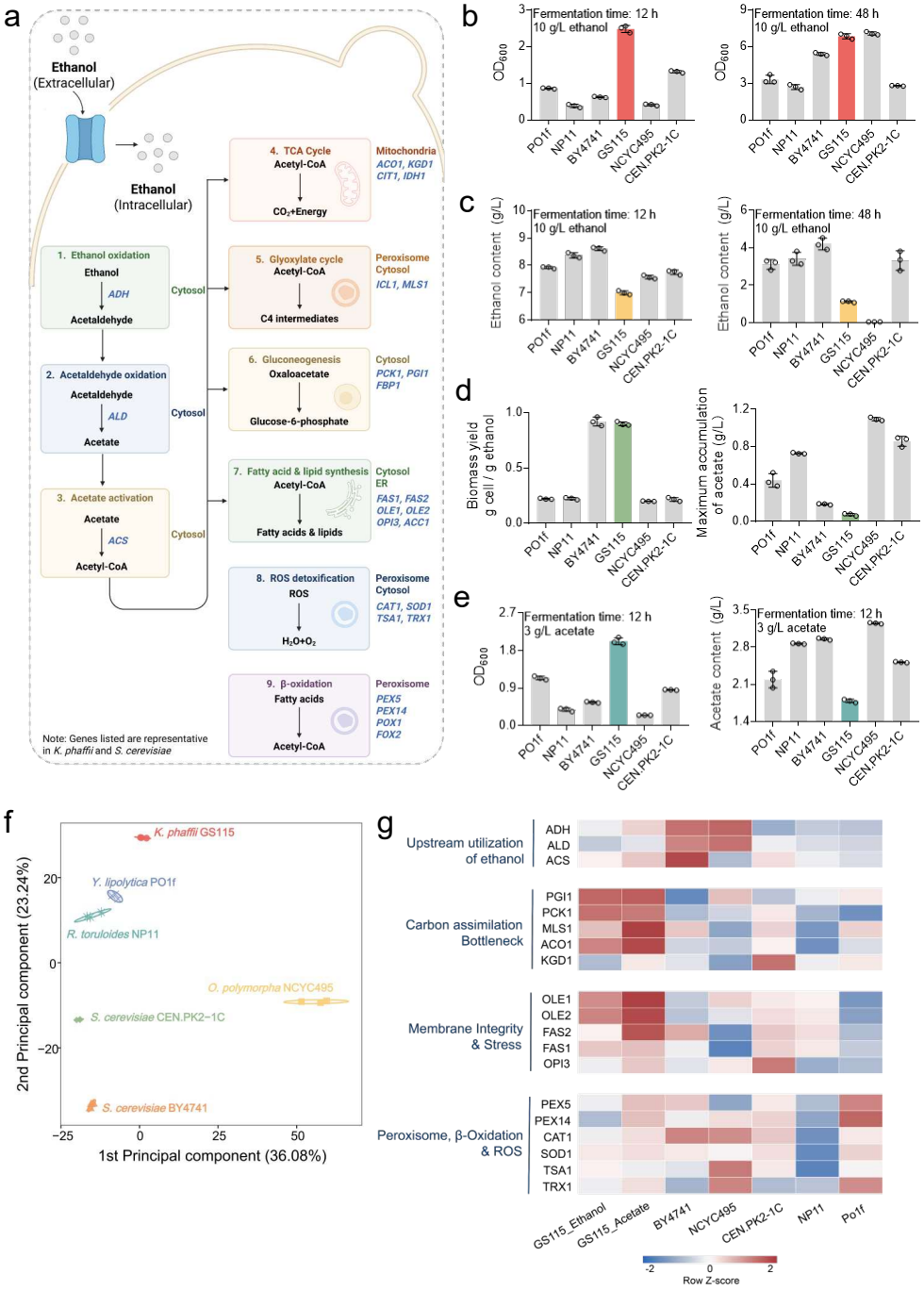

Fig. 2 | Comparative evaluation of yeast hosts for ethanol assimilation and utilization. **(a)** Schematic representation of the major metabolic modules involved in ethanol assimilation and utilization in yeast. **(b)** Growth profiles of six representative yeast strains cultivated in medium containing 10 g/L ethanol. **(c)** Residual ethanol concentrations in the cultures shown in b. **(d)** Biomass yield and maximum acetate accumulation of the six yeast strains during growth on 10 g/L ethanol. **(e)** Growth and acetate consumption of the six yeast strains cultivated in medium containing 3 g/L acetate. **(f)** PCA of metabolic phenotypes of the six yeast strains under ethanol- and acetate-utilizing conditions. **(g)** Heatmap showing the relative expression levels of key genes in the six yeast strains under ethanol- and acetate-utilizing conditions.

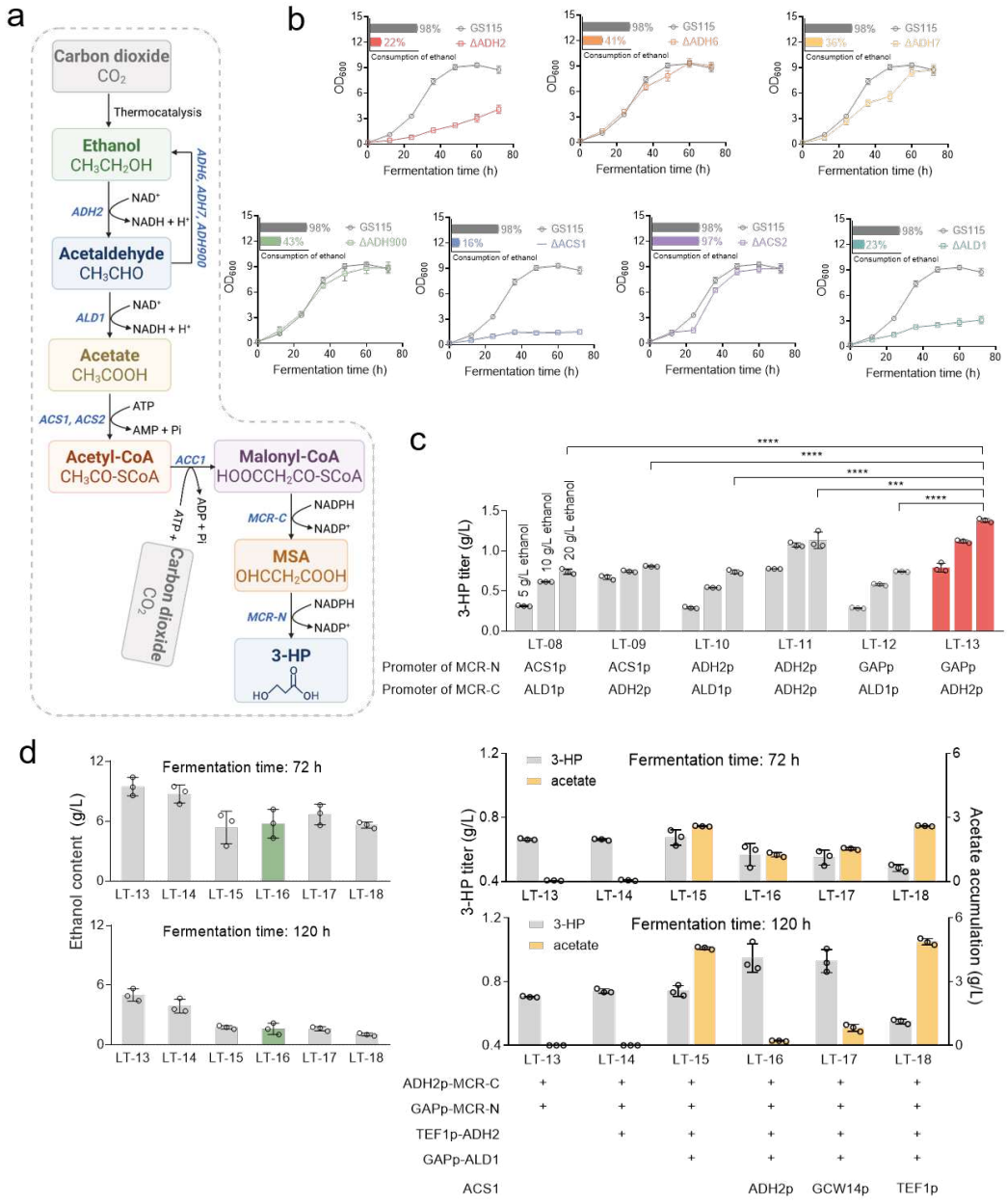

Fig. 3 | Characterization and initial optimization of an ethanol-driven 3-HP biosynthetic chassis. (a) Schematic representation of the engineered metabolic pathway from CO_2-derived ethanol to 3-HP in GS115. **(b)** Growth and residual ethanol concentrations of GS115-derived strains with individual deletions of seven genes **(c)** 3-HP production by strains carrying six promoter combinations for the expression of MCR-C and MCR-N in media containing 5 g/L, 10 g/L, 20 g/L ethanol. **(d)** Extracellular acetate, residual ethanol and 3-HP concentrations of LT-13 to LT-18 cultivated in media containing 1 g/L, 5 g/L, 10 g/L, 20 g/L ethanol for 72 h. LT-14 to LT-18 were derived from LT-13 by overexpression of ADH2, ALD1 and ACS1 using different promoter configurations. **(e)** Extracellular acetate, residual ethanol and 3-HP concentrations of LT-13 to LT-18 cultivated in media containing 1 g/L, 5 g/L, 10 g/L, 20 g/L ethanol for 120 h.

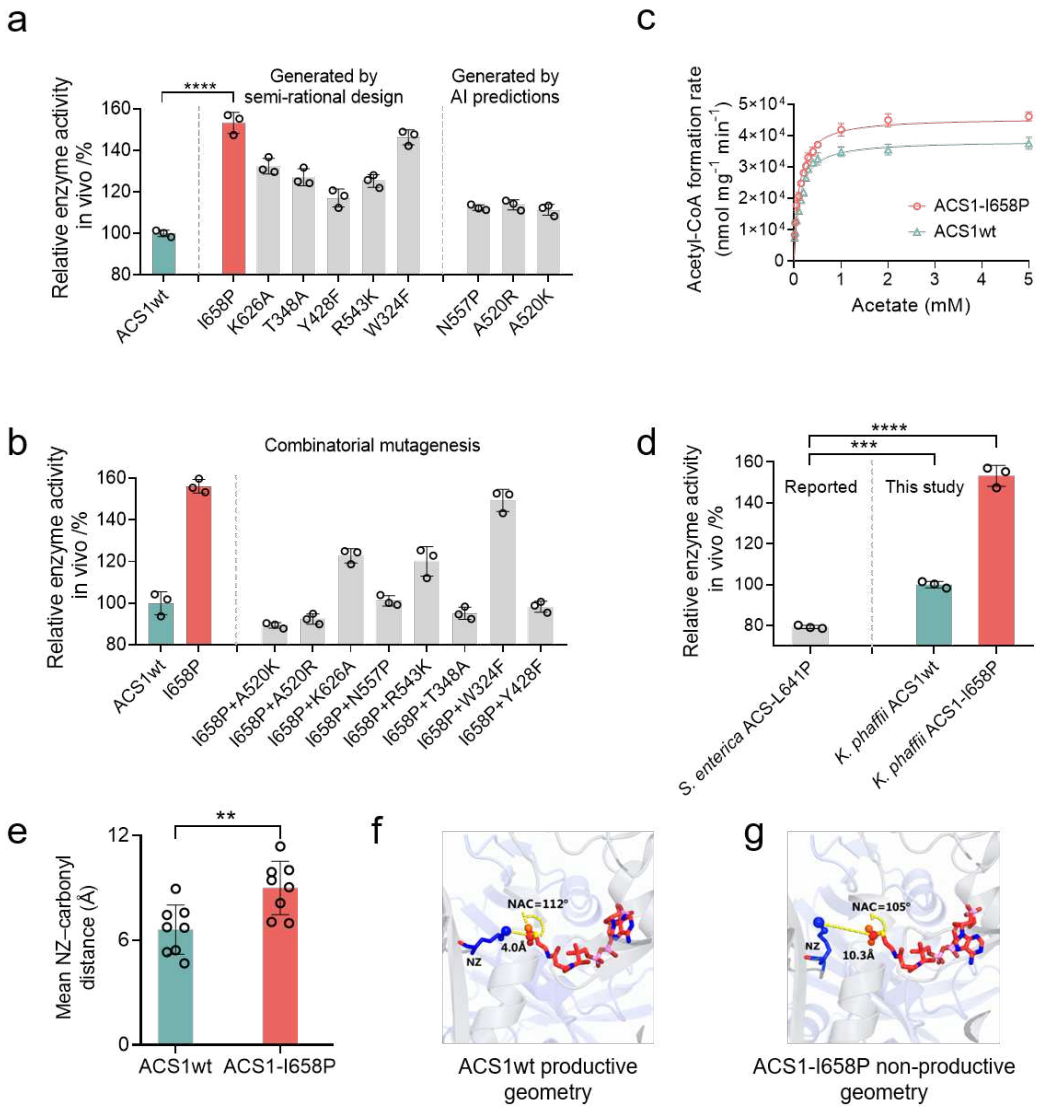

Fig. 4 | Engineering of endogenous ACS1 and structural characterization of the I658P variant. **(a)** Relative activities of ACS1 variants generated by semi-rational design, determined from 3-HP production and normalized to that of ACS1wt. **(b)** Relative activities of combinatorial ACS1 mutants containing I658P together with additional substitutions. **(c)** In vitro enzyme kinetic simulation curves of ACS1wt and ACS1-I658P. **(d)** Comparison of the relative enzymatic activities of the previously reported *S. enterica* ACS-L641P variant and K. phaffii ACS1wt and ACS1-I658P characterized in this study. **(e)** Mean distance between the K626 NZ atom and the acetyl carbonyl carbon of ACO in ACS1wt and ACS1-I658P, calculated from eight independent MD simulations. **(f)** Representative MD geometry of ACS1wt showing a productive geometry for acetyl transfer. The ACS domain is shown in gray, the GNAT domain in light purple, docked acetyl-CoA in red sticks, and K626 in blue sticks. The K626 NZ atom is positioned 4.0 Å from the acetyl carbonyl carbon of ACO, with an NZ–C–O of 112°. **(g)** Representative MD geometry of ACS1-I658P showing a non-productive geometry, in which the K626 NZ–carbonyl distance increases to 10.3 Å while the NAC angle remains 105°.

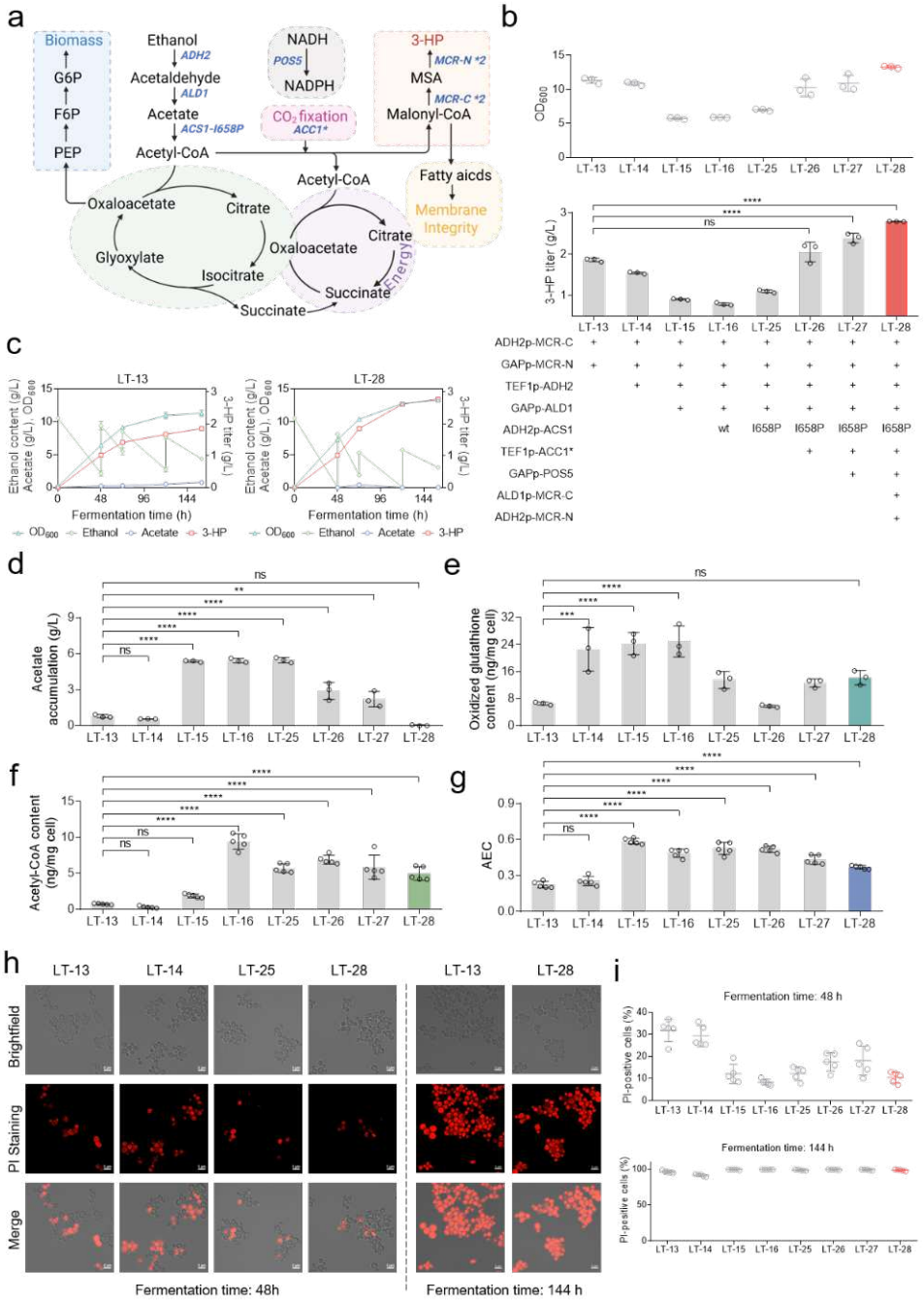

Fig. 5 | Physiological characterization of engineered strains for enhanced 3-HP production. (a) Schematic overview of the metabolic engineering strategy in GS115. **(b)** 3-HP production and OD_{600} of engineered strains during 160 h of fed-batch cultivation in shake flasks. **(c)** Time-course profiles of 3-HP production and ethanol feeding during 160 h of fed-batch cultivation of LT-13 and LT-28. **(d)** Intracellular acetyl-CoA concentrations of the eight engineered strains measured. **(e)** Intracellular oxidized glutathione concentrations of the eight engineered strains. **(f)** Intracellular ATP concentrations of the eight engineered strains. **(g)** AEC of the eight engineered strains. **(h)** PI staining of the eight engineered strains at 48 h and 144 h during ethanol fed-batch cultivation. Representative red-fluorescence microscopy images are shown; scale bars, 5 μm. **(i)** Quantification of the proportion of PI-positive cells.

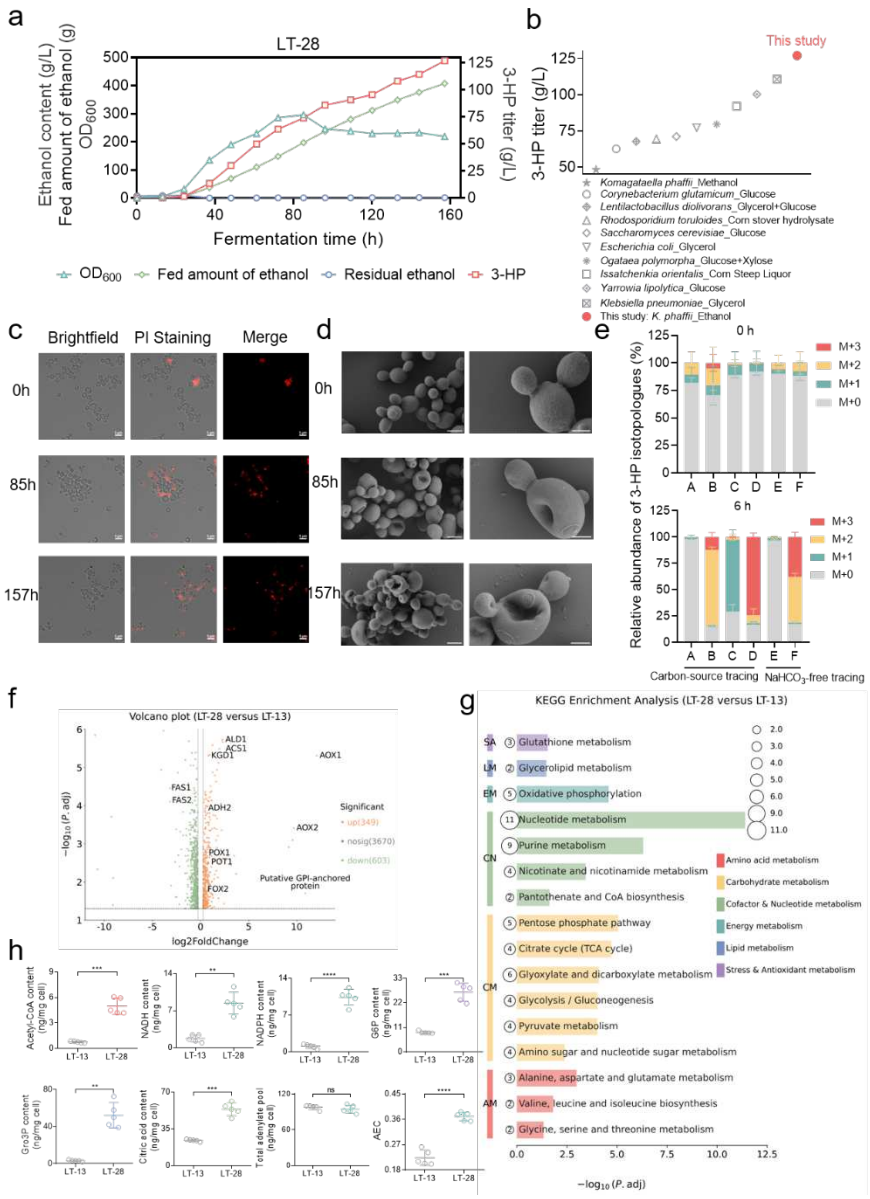

Fig. 6 | Bioreactor fermentation and multi-level characterization of the engineered strain LT-28. (a) Time-course profiles of OD_{600}, ethanol concentration, ethanol feeding quality, residual ethanol and 3-HP titer during 157 h of fed-batch cultivation of LT-28 in DasGip. **(b)** Comparison of 3-HP production achieved in this study with previously reports. More details are provided in Supplementary Table 10. **(c)** Representative PI fluorescence microscopy images of LT-28 sampled at 0 h, 85 h and 157 h during the bioreactor fermentation shown in a. Scale bars, 5 μm. **(d)** Representative SEM images of LT-28 cells sampled at 0, 85 and 157 h during the bioreactor fermentation shown in a. Scale bars, 2 μm. **(f)** Proteomic comparison of LT-28 and LT-13 shown by volcano plot. **(e)** Relative abundances of the M+0, M+1, M+2 and M+3 isotopologues of 3-HP at 0 and 6 h under the six isotope-labelling conditions; detailed experimental designs in Supplementary Table 9. Data are presented as mean ± s.d. of four independent biological replicates. **(g)** KEGG pathway enrichment analysis comparing LT-13 and LT-28 grown in ethanol-containing medium. **(h)** Intracellular levels of nine key metabolites in LT-13 and LT-28 grown in ethanol-containing medium.

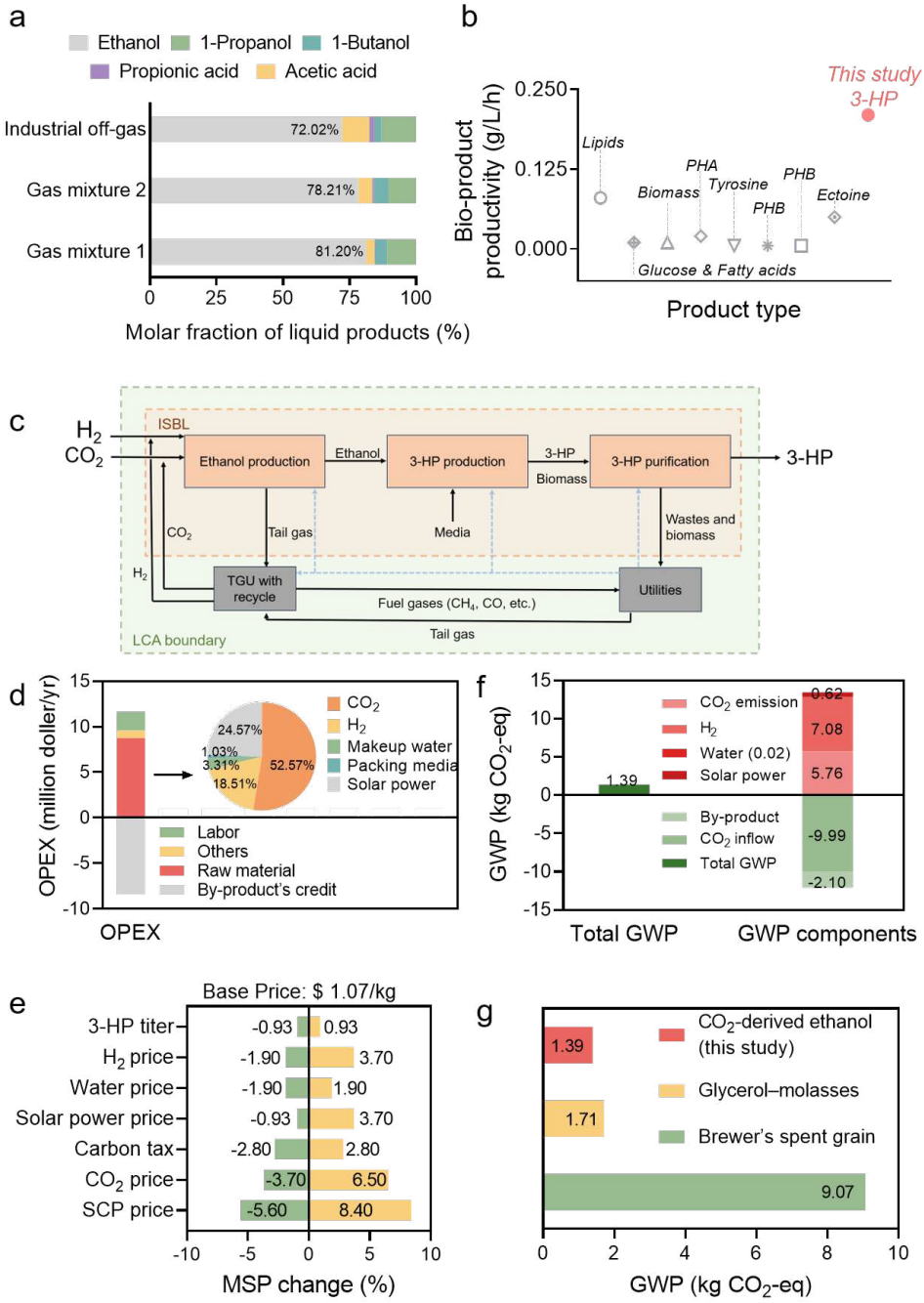

Fig. 7 | Process performance, TEA and LCA of integrated CO_2-to-3-HP production. **(a)** Liquid-product selectivity distribution for CO_2 thermocatalytic ethanol synthesis using gas mixture 1, gas mixture 2 and industrial off-gas. **(b)** Comparison of the chem–biocatalytic strategy for 3-HP synthesis developed in this study with previously reports. More details are provided in Supplementary Table 11. **(c)** Process design and system boundaries for integrated CO_2-to-3-HP production. ISBL, inside battery limits. TGU, tail-gas utilization. **(d)** OPEX and cost contribution of major inputs. **(e)** Single-point sensitivity analysis of the MSP of 3-HP in response to ±20% changes in the prices of major raw materials, utilities and the SCP co-product relative to their base-case values. **(f)** GWP and contribution analysis of the integrated process. **(g)** Comparison of GWP with previously reported 3-HP production routes.

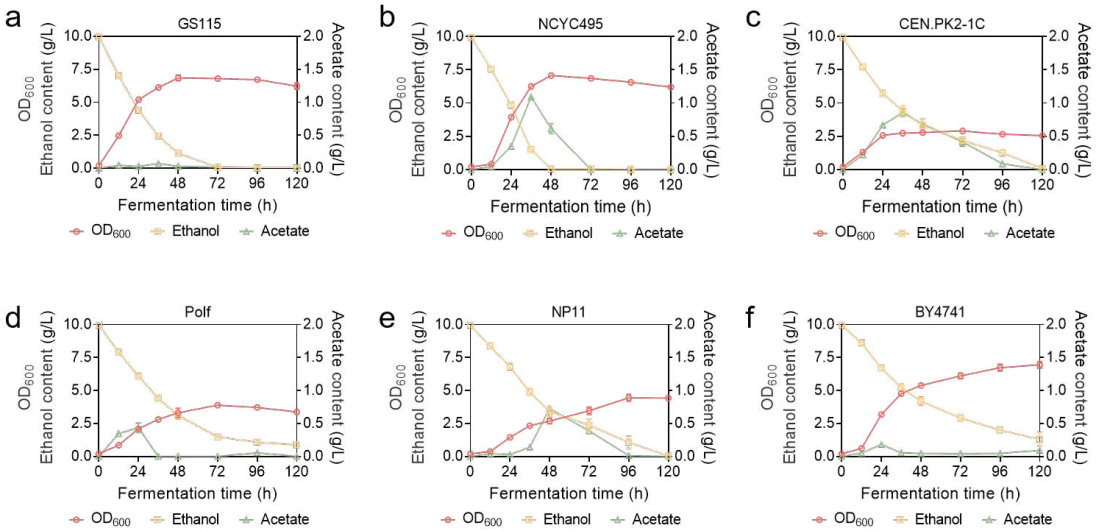

Extended Data Fig. 1 | Fermentation kinetics and ethanol utilization profiles of six representative yeast strains under 10 g/L ethanol cultivation.

a, Time-course fermentation profile of *K.phaffii* GS115 showing cell growth (OD600, red circles), ethanol consumption (g/L, yellow squares), and extracellular acetate accumulation (g/L, green triangles) over 120 h. **b**, Time-course profile of *O. polymorpha* NCYC495. **c**, Time-course profile of *S. cerevisiae* CEN.PK2-1C. **d**, Time-course profile of *Y. lipolytica* PO1f. **e**, Time-course profile of *R. toruloides* NP11. **f**, Time-course profile of *S. cerevisiae* BY4741. All strains were cultured in synthetic medium containing 10 g/L ethanol as the sole carbon source. Data are presented as mean ±s.d. (n=3 independent biological replicates).

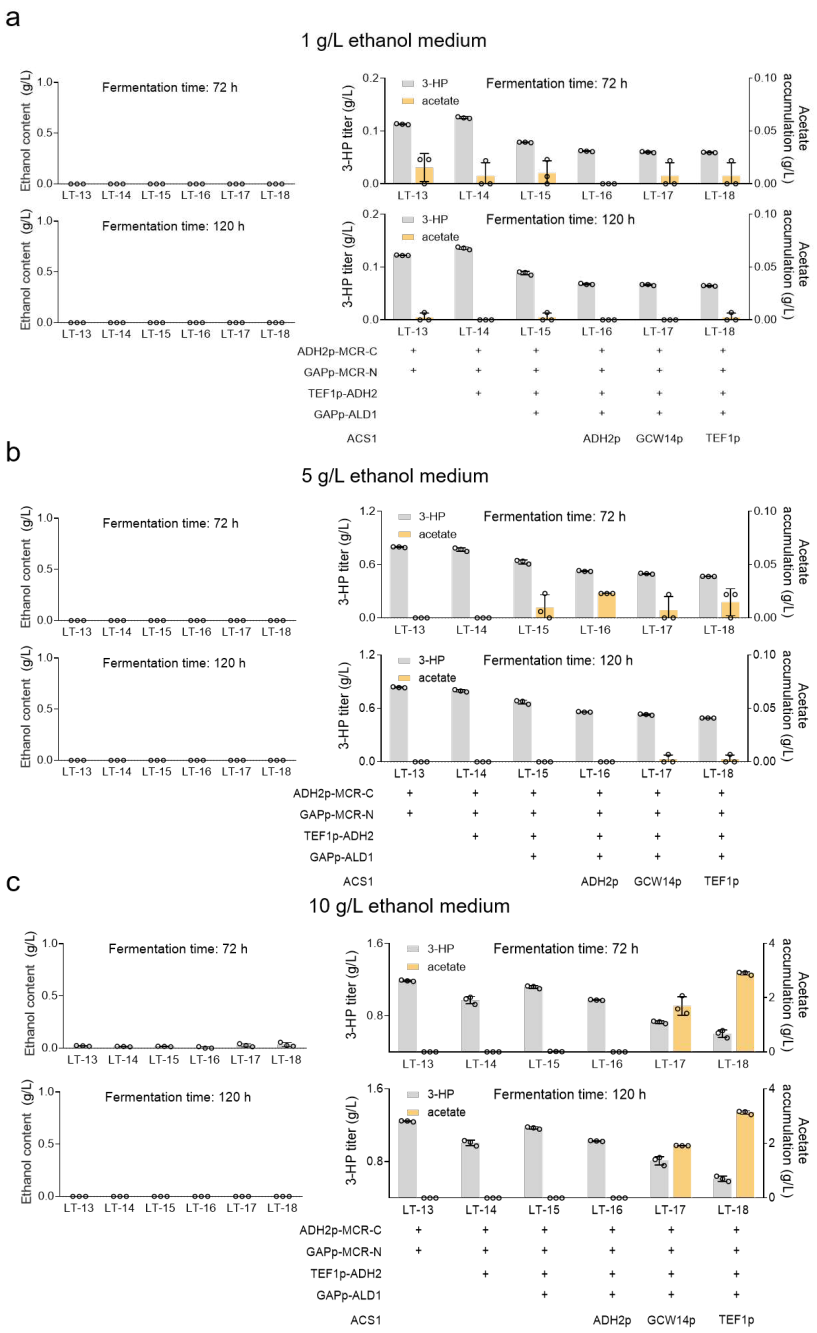

Extended Data Fig. 2 | Characterization of ethanol assimilation and 3-HP production across engineered strains under lower substrate loadings.

a, Fermentation profiles of engineered strains (LT-13 to LT-18) in media containing 1 g/L ethanol. Residual ethanol content (left panels), 3-HP titers (right panels, grey bars), and acetate accumulation (right panels, yellow bars) were determined at 72 h and 120 h of cultivation, respectively. Genotypic modifications of the respective strains—including the expression modules of MCR-C, MCR-N, ADH2, ALD1, and ACS1 under distinct promoters—are indicated at the bottom. **b**, Same as in **a**, but with 5 g/L ethanol medium. **c**, Same as in **a**, but with 10 g/L ethanol medium. Data are presented as mean ± s.d. (n = 3 independent biological replicates).

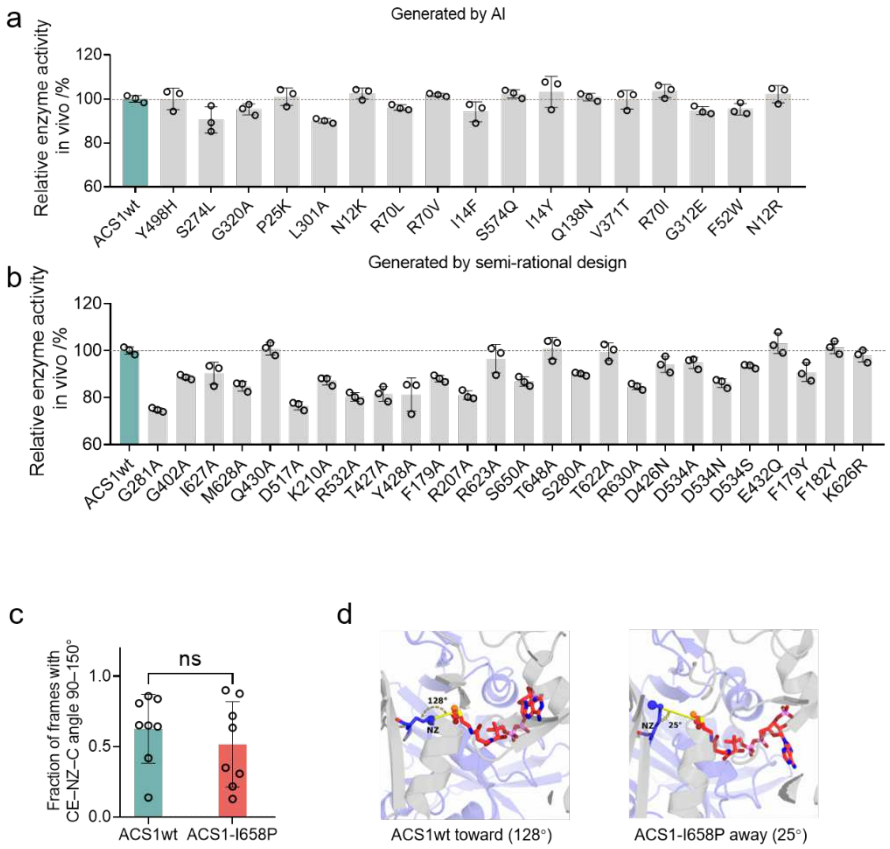

Extended Data Fig. 3 | Engineering of endogenous , *BGL1* GS115 ACS1 and characterization of variants.

a, Relative activities of 17 ACS1 variants selected by Saprot-based protein language model prediction, determined from 3-HP production after cultivation in medium containing 20 g/L ethanol for 120 h. **b**, Relative activities of 26 ACS1 variants selected by semi-rational design, determined from 3-HP production after cultivation in medium containing 20 g/L ethanol for 120 h. Data are presented as mean ±s.d. (n=3 independent biological replicates). **c**, Fraction of MD simulation frames with a CE–NZ–C angle of 90–150°, defined as the “toward ACO” orientation. Points represent independent MD replicas; bars show the mean and error bars indicate s.d.; ns, not significant. **d**, Representative MD snapshots of ACS1wt in a toward-ACO orientation (128°) and ACS1-I658P in an away-from-ACO orientation (25°). The ACS domain is shown in gray, the GNAT domain in light purple, docked acetyl-CoA (ACO) in red sticks and K626 in blue sticks. The K626 NZ atom is the terminal nitrogen of the lysine side chain and represents the nucleophilic amine that attacks the acetyl carbonyl carbon of ACO. Yellow dashed arcs indicate the CE–NZ–C angle. The CE–NZ–C angle is defined by the K626 C atom (CE), the terminal N atom of the K626 lysine side chain (NZ), and the acetyl carbonyl carbon of ACO (C).

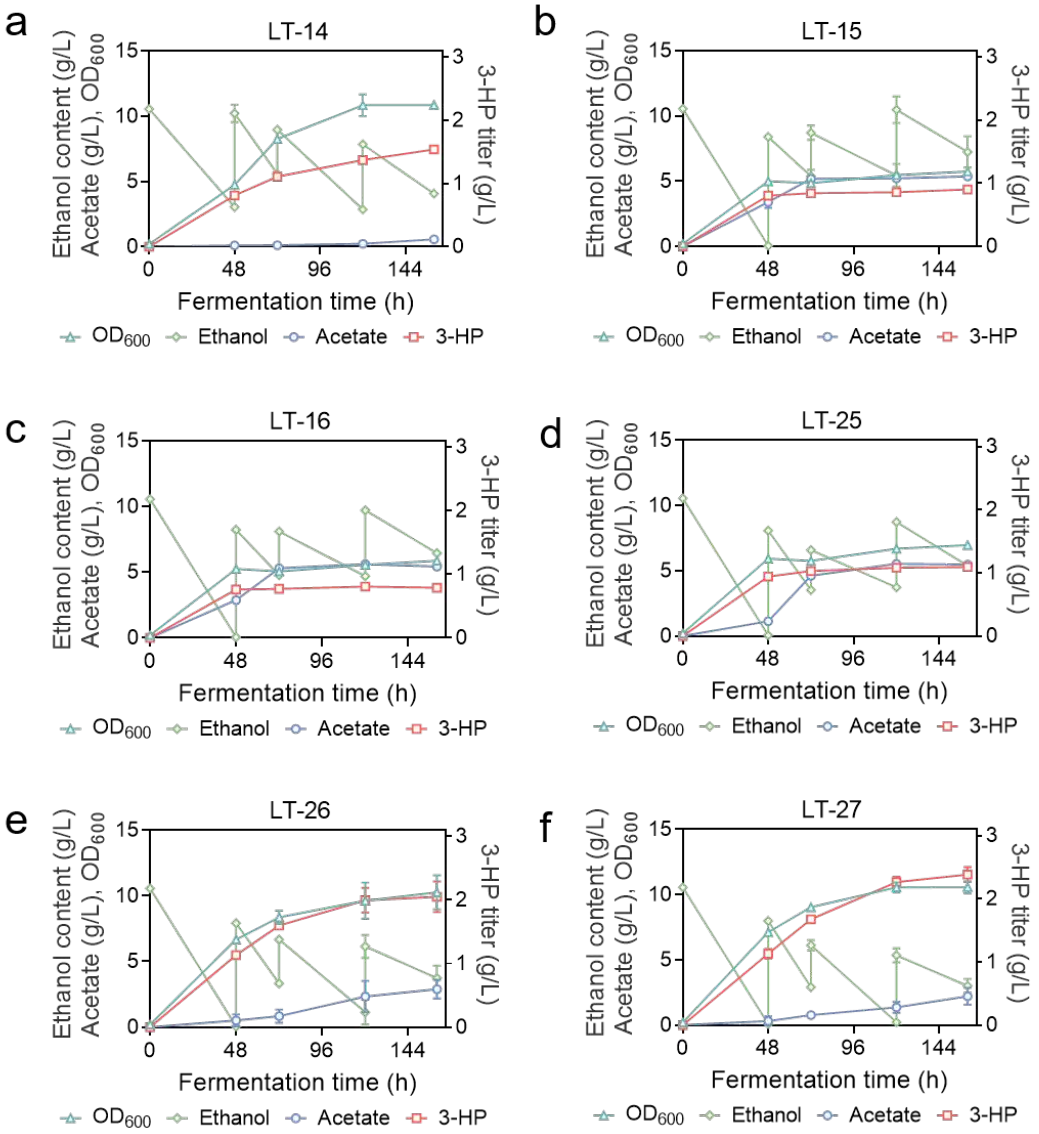

Extended Data Fig. 4 | Time-course profiles of six engineered strains during 160 h of fed-batch shake-flask cultivations.

a, Time-course profiles of cell growth (OD_{600}, cyan triangles), residual ethanol content (green diamonds), acetate accumulation (blue circles), and 3-HP titer (red squares) for strain LT-14 during 160 h of fed-batch cultivation in shake flasks. The initial ethanol concentration was set at 10 g/L. Intermittent pulse feeding of pure ethanol (0.2–0.5 mL) paired with an equal volume of 2.5xYNB solution was initiated at 48 h and maintained every 24–48 h. **b**, Same as in a, time-course profile of strain LT-15. **c**, Same as in a, time-course profile of strain LT-16. **d**, Same as in a, time-course profile of strain LT-25. **e**, Same as in a, time-course profile of strain LT-26. f, Same as in a, time-course profile of strain LT-27. Data are presented as mean ± s.d. (n = 3 independent biological replicates).

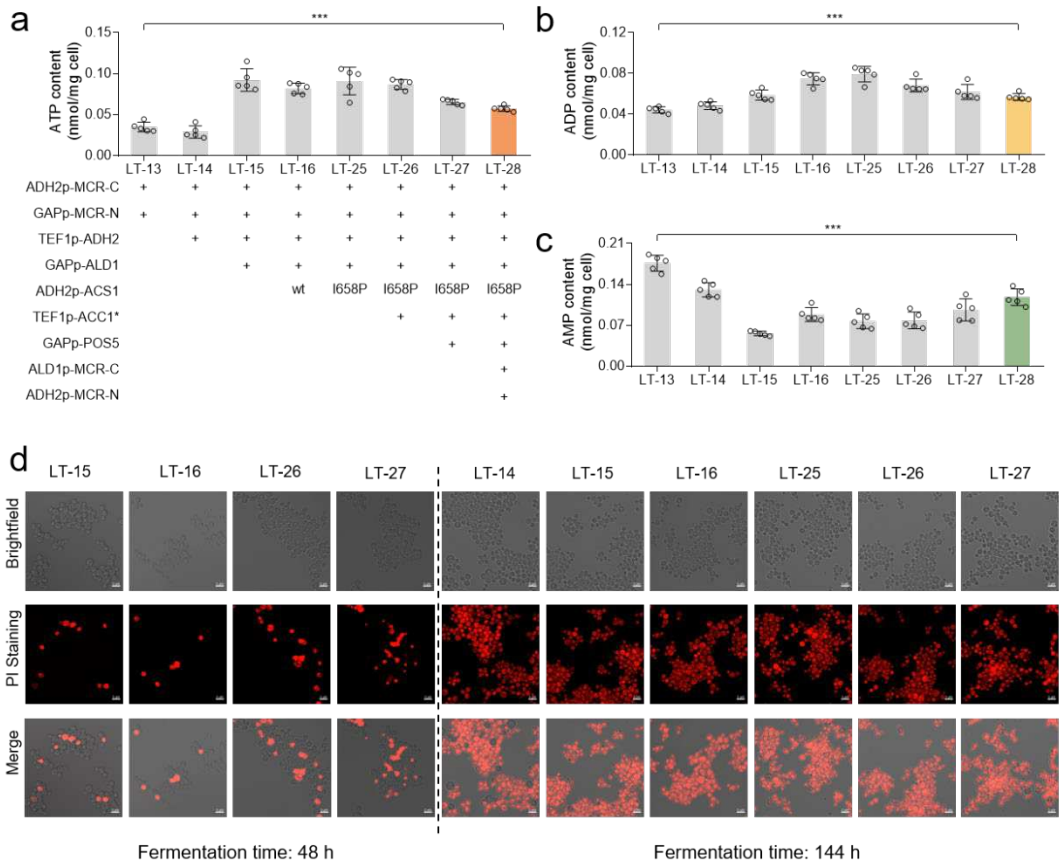

Extended Data Fig. 5 | Intracellular adenylate levels and cell membrane integrity of eight engineered strains during 160 h of fed-batch shake-flask cultivations.

a, Intracellular ATP content in eight engineered strains (LT-13 to LT-28). Genotypic modifications of each strain—including the progressive integration of MCR-C, MCR-N, ADH2, ALD1, ACS1 (wild-type or I658P mutant), ACC1*, and POS5 expression modules under specified promoters—are indicated at the bottom. **b**, Intracellular ADP content in the eight engineered strains. **c**, Intracellular AMP content in the eight engineered strains. Data in a-c are presented as mean ± s.d. (n = 5 independent biological replicates). Statistical significance was determined using one-way ANOVA with Tukey's post-hoc test (***$P < 0.001$). **d**, PI staining depicting membrane integrity of engineered strains at 48 h and 144 h during 160 h fed-batch shake-flask cultivations. Brightfield images (top), PI fluorescence staining images (middle), and merged overlays (bottom) are shown. Scale bars, 5 μm. Representative images are from n=5 independent experiments with similar results.

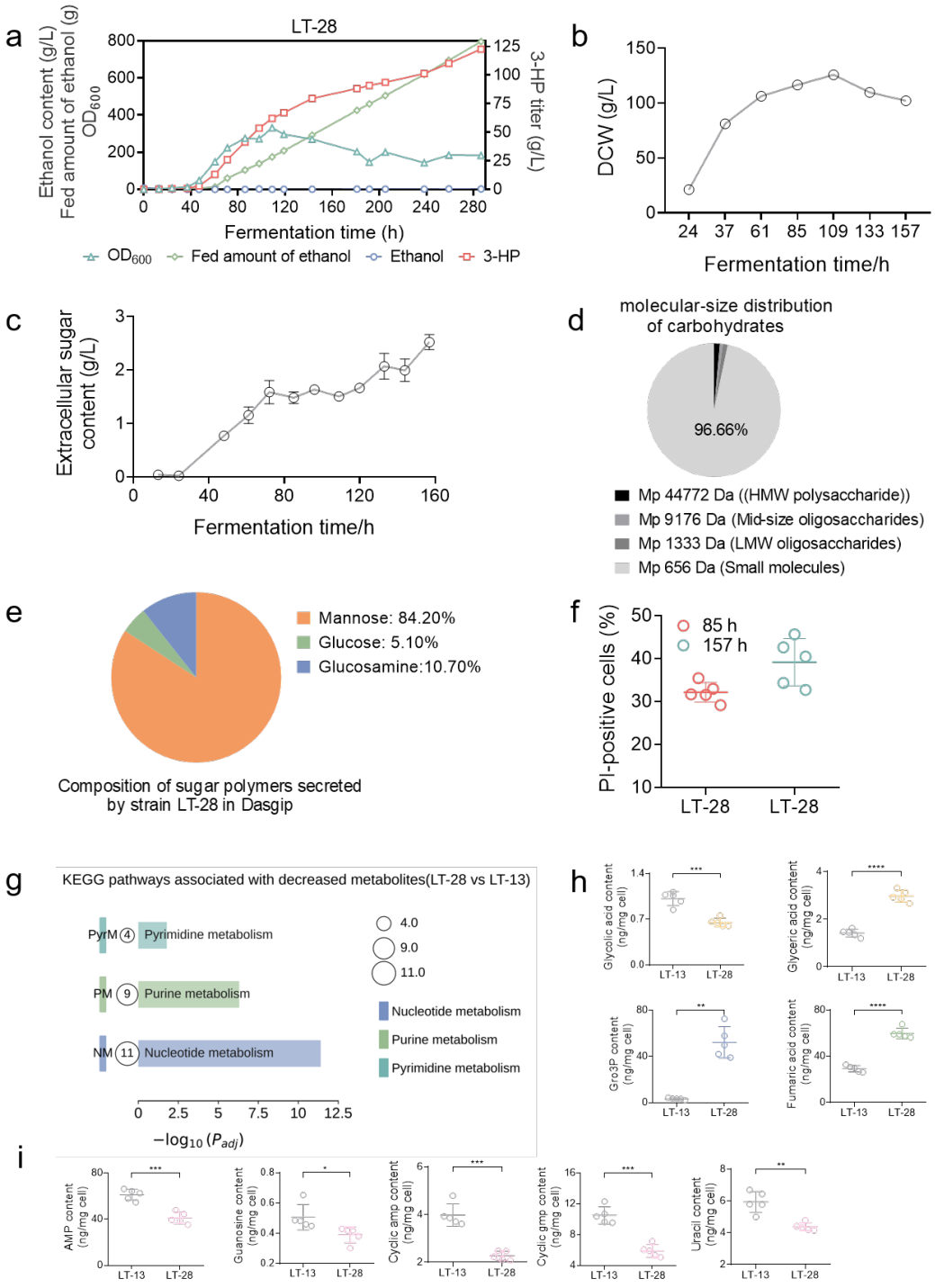

Extended Data Fig. 6 | Scale-up performance of strain LT-28 in a bioreactor and comparative intracellular metabolomic profiling.

a, Initial fed-batch fermentation profile of strain LT-28 in a Dasgip bioreactor. Cultivation was performed with an initial OD_{600} of 0.810 in 8 g/L YNE medium, with pH controlled at 5.6 and ethanol feeding triggered by DO levels > 40%. b–f, Characterization of extracellular carbohydrate secretion and cell viability of strain LT-28 during bioreactor cultivation corresponding to the fermentation trial shown in Fig. 6a. **b**,

DCW profile. **c**, Extracellular total sugar content determined by the anthrone-sulfuric acid assay. Data are presented as mean ± s.d. (n= 3 biological replicates). **d**, Molecular-size distribution of extracellular carbohydrates analyzed by HPGPC. Values represent peak area percentages. **e**, Molar percentage composition of monosaccharides in secreted oligosaccharides and polysaccharides determined by HPAEC-PAD. **f,** Proportions of propidium iodide (PI)-positive cells sampled at 85 h and 157 h. Center line indicates mean (n = 5 biological replicates). **g,** KEGG pathway enrichment analysis ($-\log_{10}P.$ adj) of differential intracellular metabolites between strain LT-28 and control strain LT-13. Selected pathways contain representative metabolites that decreased in LT-28 (including AMP, guanosine, cAMP, cGMP, and uracil). Bubble size represents the total number of differential metabolites mapped to each pathway. **h, i,** Comparative levels of representative upregulated (h) and downregulated (i) intracellular metabolites between strains LT-13 and LT-28. Data are presented as mean ± s.d. (n = 5 biological replicates). Statistical significance was calculated using two-tailed unpaired t-test with Welch's correction. ($^{*}P < 0.05$, $^{**}P < 0.01$, $^{***}P < 0.001$, $^{****}P < 0.0001$).

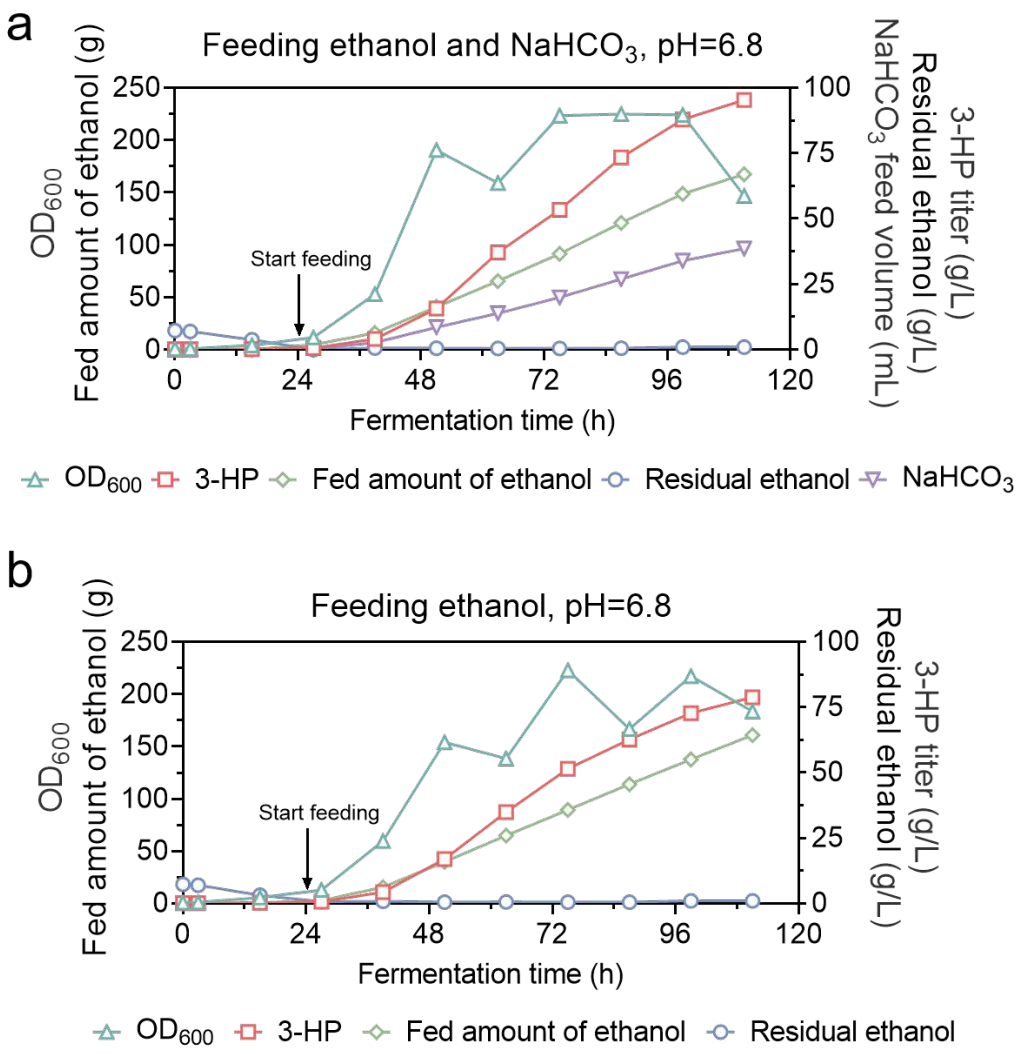

Extended Data Fig. 7 | Effect of $NaHCO_3$ supplementation on fed-batch production of 3-HP by engineered strain LT-28.

a, Fed-batch fermentation of LT-28 using ethanol as the sole carbon source. **b**, Fed-batch fermentation of LT-28 supplemented with $NaHCO_3$ (50 mM in the initial medium and 300 mM in the feeding solution). Both fermentations were performed at pH 6.8 using the same DO-responsive ethanol-feeding strategy. Time-course profiles show OD_{600}, 3-HP titer, ethanol feeding and $NaHCO_3$ feeding. Data represent one independent bioreactor fermentation per condition (n = 1).

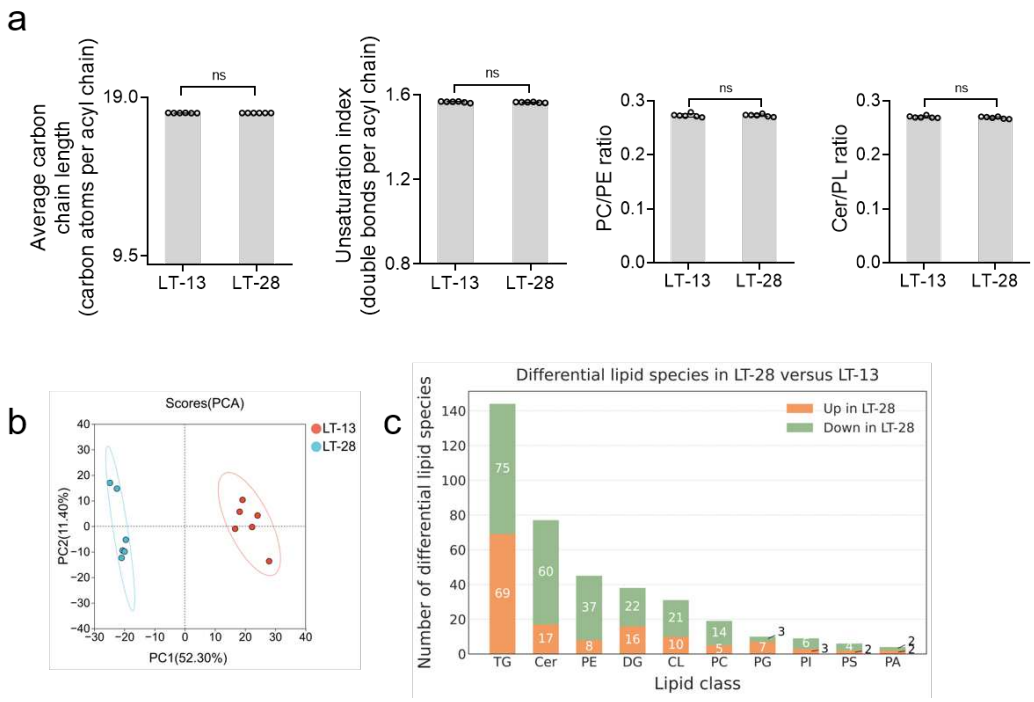

Extended Data Fig. 8 | Lipidomic profiling of LT-13 and LT-28 during growth on ethanol.

a, Comparison of global lipid structural indices between LT-13 and LT-28, including average acyl-chain length (ACL), unsaturation index (UI), phosphatidylcholine-to-phosphatidylethanolamine ratio (PC/PE) and ceramide-to-phospholipid ratio (Cer/PL). ACL and UI were calculated as abundance-weighted averages of phospholipid species, with ACL expressed as the number of carbon atoms per acyl chain and UI as the number of double bonds per acyl chain. PC/PE and Cer/PL were calculated from the summed normalized abundances of the corresponding lipid classes. Data are shown as individual biological replicates (n = 6) with bars representing the mean. Statistical significance was assessed using two-sided Welch's *t*-tests; ns, not significant. **b**, PCA of the lipidomic profiles in positive-ion mode of LT-13 and LT-28. Each point represents an independent biological replicate (n = 6). The percentages indicate the variance explained by the first two principal components. Ellipses indicate 95% confidence intervals. **c**, Distribution of differential lipid species between LT-28 and LT-13 across major lipid classes. Bars show the numbers of lipid species that were increased or decreased in LT-28 relative to LT-13. TG, triglyceride; Cer, ceramide; PE, phosphatidylethanolamine; DG, diglyceride; CL, cardiolipin; PC, phosphatidylcholine; PG, phosphatidylglycerol; PI, phosphatidylinositol; PS, phosphatidylserine; PA, phosphatidic acid.

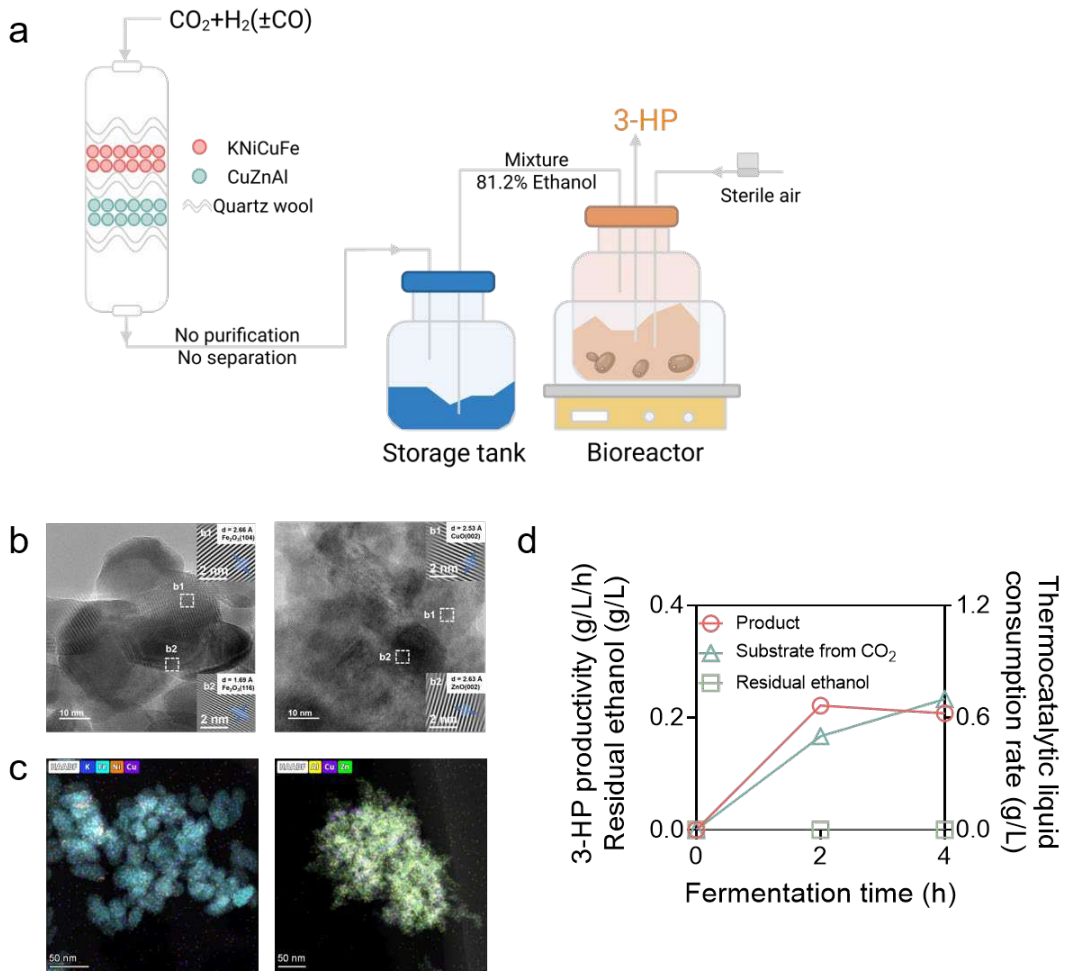

Extended Data Fig. 9 | Coupled thermocatalytic-biological conversion of CO_2 to 3-HP by engineered strain LT-28.

a, Schematic of the integrated CO_2-to-3-HP system. CO_2/H_2 (±CO) passes through a dual-bed thermocatalytic reactor to generate ethanol-rich liquid products, which are directly delivered to the LT-28 bioreactor for 3-HP synthesis without purification. **b**, HRTEM micrographs of the KNiCuFe (left) and CuZnAl (right) catalysts. Insets b1 and b2 display lattice-resolved crystalline features. **c**, Elemental mapping showing elemental distribution of KNiCuFe (left) and CuZnAl (right) catalyst particles. **d**, Time-dependent profiles of 3-HP productivity, substrate consumption rate and residual ethanol concentration during the coupled bioconversion.

Supplementary Files

This is a list of supplementary files associated with this preprint. Click to download.

- SupplementaryInformation.pdf